

2

NAVAL POSTGRADUATE SCHOOL

Monterey, California

AD-A253 021



THESIS

DESIGN AND FABRICATION OF A FIBER-OPTIC
INTERFEROMETRIC
ACCELEROMETER SYSTEM

by

Mary Beth A. Chipkevich

March 1992

Thesis Advisor
Co-Advisor

David L. Gardner
David A. Brown

**Approved for public release
distribution unlimited.**

92-19037



015

48

Unclassified

security classification of this page

REPORT DOCUMENTATION PAGE				
1a Report Security Classification Unclassified		1b Restrictive Markings		
2a Security Classification Authority		3 Distribution Availability of Report Approved for public release; distribution is unlimited.		
2b Declassification Downgrading Schedule				
4 Performing Organization Report Number(s)		5 Monitoring Organization Report Number(s)		
6a Name of Performing Organization Naval Postgraduate School	6b Office Symbol <i>(if applicable)</i> 33	7a Name of Monitoring Organization Naval Postgraduate School		
6c Address <i>(city, state, and ZIP code)</i> Monterey, CA 93943-5000		7b Address <i>(city, state, and ZIP code)</i> Monterey, CA 93943-5000		
8a Name of Funding Sponsoring Organization	8b Office Symbol <i>(if applicable)</i>	9 Procurement Instrument Identification Number		
8c Address <i>(city, state, and ZIP code)</i>		10 Source of Funding Numbers		
		Program Element No	Project No	Task No
		Work Unit	Accession No	
11 Title <i>(include security classification)</i> DESIGN AND FABRICATION OF A FIBER-OPTIC INTERFEROMETRIC ACCELEROMETER SYSTEM				
12 Personal Author(s) Mary Beth A. Chipkevich				
13a Type of Report Master's Thesis		13b Time Covered From To	14 Date of Report <i>(year, month, day)</i> March 1992	15 Page Count 88
16 Supplementary Notation The views expressed in this thesis are those of the author and do not reflect the official policy or position of the Department of Defense or the U.S. Government.				
17 Cosati Codes		18 Subject Terms <i>(continue on reverse if necessary and identify by block number)</i>		
Field	Group	Subgroup	Fiber optic, Interferometric, Mach-Zender, Flexural Disk	
19 Abstract <i>(continue on reverse if necessary and identify by block number)</i>				
<p>Two fiber-optic accelerometer designs are presented. The first accelerometer was constructed using two flexural disks between which is a center spindle. Six uniformly spaced screws fasten the disk assembly to a circular, hollow base housing fiber-optic couplers and splices and providing fiber access. The disk edge is elastically restrained. A flat spirally wound coil of optical fiber is bonded to one surface of each disk. Disk surface strains, caused by acceleration, are detected in a push-pull fashion by fiber coils comprising the legs of a Mach-Zender optical interferometer. This sensor demonstrated an acceleration sensitivity of 2.3 ± 0.1 rad/g over a bandwidth of 150-475 Hz. The resonance frequency was 1.22 ± 0.05 kHz.</p> <p>The second accelerometer design described exploits the benefits of using a disk material having a significantly slower sound speed than aluminum; in general, a slower sound speed increases the acceleration sensitivity and decreases the resonance frequency. One polycarbonate disk with a simply supported edge condition is fastened between an aluminum cap and an aluminum housing base secured with six uniformly spaced screws. One flat fiber coil in each Mach-Zender interferometer leg was bonded to each disk surface. This sensor demonstrated an acceleration sensitivity of 56.9 ± 4.0 rad/g over a bandwidth of 30-950 Hz. The resonance frequency was 1.7 ± 0.05 kHz.</p> <p>Both sensors are compatible with the symmetric 3x3 demodulator developed at the Naval Postgraduate School. The second sensor and demodulator have been integrated and constitute a sensor system, but testing has not been completed.</p>				
20 Distribution Availability of Abstract		21 Abstract Security Classification		
<input checked="" type="checkbox"/> unclassified unlimited <input type="checkbox"/> same as report <input type="checkbox"/> DTIC users		Unclassified		
22a Name of Responsible Individual David L. Gardner		22b Telephone <i>(include Area code)</i> (408) 646-2768	22c Office Symbol 54Ss	

Approved for public release; distribution is unlimited.

Design and Fabrication of a Fiber-Optic Interferometric
Accelerometer System

by

Mary Beth A. Chipkevich
Lieutenant, United States Navy
B.S., United States Naval Academy, 1984

Submitted in partial fulfillment of the
requirements for the degree of

MASTER OF SCIENCE IN ENGINEERING ACOUSTICS

from the

NAVAL POSTGRADUATE SCHOOL
March 1992

Author:

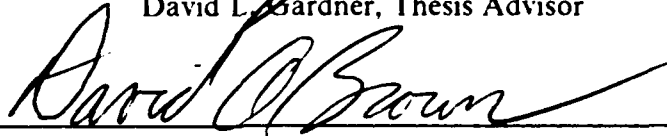


Mary Beth A. Chipkevich

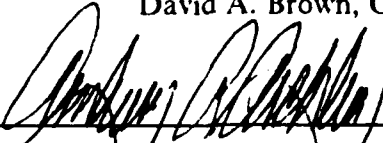
Approved by:



David L. Gardner, Thesis Advisor



David A. Brown, Co-Advisor



Anthony A. Atchley, Chairman,
Engineering Acoustics Academic Committee

ABSTRACT

Two fiber-optic accelerometer designs are presented. The first accelerometer was constructed using two flexural disks between which is a center spindle. Six uniformly spaced screws fasten the disk assembly to a circular, hollow base housing fiber-optic couplers and splices and providing fiber access. The disk edge is elastically restrained. A flat spirally wound coil of optical fiber is bonded to one surface of each disk. Disk surface strains, caused by acceleration, are detected in a push-pull fashion by fiber coils comprising the legs of a Mach-Zender optical interferometer. This sensor demonstrated an acceleration sensitivity of $2.3 \pm 0.1 \text{ rad/g}$ over a bandwidth of 150-475 Hz. The resonance frequency was $1.22 \pm 0.05 \text{ kHz}$.

The second accelerometer design described exploits the benefits of using a disk material having a significantly slower sound speed than aluminum; in general, a slower sound speed increases the acceleration sensitivity and decreases the resonance frequency. One polycarbonate disk with a simply supported edge condition is fastened between an aluminum cap and an aluminum housing base secured with six uniformly spaced screws. One flat fiber coil in each Mach-Zender interferometer leg was bonded to each disk surface. This sensor demonstrated an acceleration sensitivity of $56.9 \pm 4.0 \text{ rad/g}$ over a bandwidth of 30-950 Hz. The resonance frequency was $1.7 \pm 0.05 \text{ kHz}$.

Both sensors are compatible with the symmetric 3x3 demodulator developed at the Naval Postgraduate School. The second sensor and demodulator have been integrated and constitute a sensor system, but testing has not been completed.

Accession For	
NTIS GRA&I	<input checked="" type="checkbox"/>
DTIC TAB	<input type="checkbox"/>
Unannounced	<input type="checkbox"/>
Justification _____	
By _____	
Distribution/ _____	
Availability Codes	
Dist	Avail and/or Special
A-1	

TABLE OF CONTENTS

I. INTRODUCTION	1
A. SCOPE	1
B. CONVENTIONAL ACCELERATION SENSORS	1
1. Background	1
2. Conventional Piezoelectric Accelerometers	2
3. Conventional Piezoresistive Strain Gage Accelerometers	5
4. Conventional Strain Gage Accelerometers	6
C. FIBER-OPTIC INTERFEROMETRIC SENSORS	6
1. Michelson Fiber-Optic Interferometer	7
2. Mach-Zender Fiber-Optic Interferometer	8
3. Fiber-Optic Accelerometers	9
II. MECHANICAL THEORY OF FLEXURAL DISKS	11
A. BOUNDARY CONDITIONS OF THIN DISKS	11
1. Simply Supported	12
2. Clamped	12
3. Free	12
4. Elastically Restrained	12
5. Comparisons Between Boundary Conditions	12
B. SURFACE STRAIN DEFORMATION OF THIN DISKS	14
1. Simply Supported	15
2. Clamped	15
C. RESONANCE FREQUENCY	16
1. Simply Supported	16
2. Clamped	16
3. Disk with Stepped Thickness and/or Added Mass	17
a. Radius and Mass Ratios Approach	18
b. Continuity of Zones Approach	21
c. Ritz Method Approach	22
D. PHASE MODULATIONS INDUCED IN OPTICAL-FIBERS	24
1. Optical Fiber Strain Induced by Flexural Disk Strain	24

a.	Simply Supported Disk	25
b.	Clamped Disk	26
2.	Acceleration Sensitivity	26
a.	Simply Supported Uniform Disk	27
b.	Clamped Uniform Disk	27
3.	Figures of Merit	28
4.	Phase Modulation and Demodulation of Mach-Zender Interferometers	35
a.	Phase Modulated Intensities with a 3 x 3 Coupler	35
b.	Symmetric 3x3 Coupler Based Demodulator	36
III.	SENSOR DESIGN, CONSTRUCTION, AND PERFORMANCE	41
A.	SENSOR DESIGN	41
1.	Dual Aluminum Disk (NPS3) Design	41
2.	Polycarbonate Disk (NPS4) Design	43
B.	SENSOR CONSTRUCTION	46
C.	PERFORMANCE MEASUREMENT PROCEDURES	49
1.	Resonance Frequency Measurement	49
2.	Acceleration Sensitivity Measurement	51
D.	OBSERVED PERFORMANCE	56
1.	Dual Aluminum Disk (NPS3) Design	56
2.	Polycarbonate Disk (NPS4) Design	58
IV.	CONCLUSIONS AND RECOMMENDATIONS	62
A.	CONCLUSIONS	62
1.	Performance	62
2.	Design Concerns	62
B.	RECOMMENDATIONS	64
APPENDIX A.	SENSOR ASSEMBLY AND PACKAGING	65
A.	INTERFEROMETER ASSEMBLY	65
B.	SENSOR PACKAGING	65
APPENDIX B.	DATA SHEETS	67
LIST OF REFERENCES	73

LIST OF REFERENCES 73

INITIAL DISTRIBUTION LIST 75

LIST OF TABLES

Table 1.	COMPARISON OF BOUNDARY CONDITIONS	13
Table 2.	SIMPLY SUPPORTED EIGENVALUES	16
Table 3.	STEPPED DISK RESONANCE FREQUENCIES	22
Table 4.	SIMPLY SUPPORTED ACCELEROMETER FIGURES OF MERIT	29
Table 5.	CLAMPED ACCELEROMETER FIGURES OF MERIT	29
Table 6.	SENSITIVITY COMPARISONS	32
Table 7.	COMPARISON OF POLYCARBONATE DISKS	32
Table 8.	COMPARISON OF LUCITE DISKS	32
Table 9.	COMPARISON OF ALUMINUM DISKS	32
Table 10.	OPTICAL FIBER COMPONENTS	48
Table 11.	MECHANICAL CHARACTERISTICS	48
Table 12.	COMPARISON OF ACCELEROMETER PERFORMANCES	62

LIST OF FIGURES

Figure 1.	Lumped Parameter Representation of an Accelerometer	2
Figure 2.	Accelerometer Frequency Response for Different Quality Factors	4
Figure 3.	Piezoresistive Strain Gage Accelerometer	5
Figure 4.	Michelson fiber-optic interferometer	8
Figure 5.	Mach-Zender fiber-optic interferometer	9
Figure 6.	Uniform Circular Disk	11
Figure 7.	Elastically Restrained Model	13
Figure 8.	Non-Uniform Circular Disks	18
Figure 9.	Critical Mass Ratios	20
Figure 10.	Critical Radius Ratios	21
Figure 11.	Zones of an Axisymmetric Disk	22
Figure 12.	Disk and Fiber Coil Radii	24
Figure 13.	Illustration of Interfering Electric Field Vectors	35
Figure 14.	Theoretical 3x3 Phase Modulated Intensities	36
Figure 15.	Algorithm for the Symmetric Demodulator.	37
Figure 16.	Cross-sectional View of the Dual Aluminum Disk Design	42
Figure 17.	Illustration of the Top and Bottom Aluminum Disks, NPS3 Design	44
Figure 18.	Cross-sectional View of the Polycarbonate Disk Design	45
Figure 19.	Coil Winding Jig	46
Figure 20.	Photograph of Dual-Aluminum Disk Accelerometer (NPS3)	47
Figure 21.	Photograph of Optical Fiber Coil Epoxied to Aluminum Disk (NPS3)	47
Figure 22.	Photograph of Brass Spindel on Bottom Aluminum Disk (NPS3)	48
Figure 23.	Photograph of Polycarbonate Disk Accelerometer (NPS4)	48
Figure 24.	Apparatus to Measure The Resonance Frequency	50
Figure 25.	Photodetector Response Measurement Induced Phase Modulations	51
Figure 26.	Apparatus Used to Measure the Acceleration Sensitivity	53
Figure 27.	Acceleration Sensitivity Measurement, NPS3	54
Figure 28.	Acceleration Sensitivity Measurement, NPS4	55
Figure 29.	Normalized Acceleration Sensitivity, NPS3	57
Figure 30.	Normalized Acceleration Sensitivity with Theory, NPS3	58
Figure 31.	Two Modes of Vibration of a Disk	59

Figure 32. Normalized Acceleration Sensitivity, NPS4	60
Figure 33. Normalized Acceleration Sensitivity with Theory, NPS4	61

ACKNOWLEDGEMENTS

Foremost among the many people who provided assistance in completing this thesis, I wish to thank my co-advisors, Dr. David Gardner and Dr. David Brown. My co-advisors provided tremendous guidance and technical insight throughout the preparation of this thesis. Undoubtedly, their extensive knowledge, patience, confidence in my abilities, and enthusiasm for experimental research were pivotal towards the completion of this thesis.

I would also like to thank Dr. Robert Keolian, Dr. Alan Coppens, LT Daphne Kapolka, David Bartlett, and LT Kevin Grundy, for their explanations and assistance at various odd hours of the day, and St. Anthony, for helping me to find several pieces of lab equipment and other items which I misplaced throughout the construction and testing of the sensors.

Thank you to everyone who provided assistance!

I. INTRODUCTION

A. SCOPE

The goal of this work is to design, construct, and evaluate the performance of an interferometric fiber-optic accelerometer utilizing a 3x3 coupler and a symmetric analog demodulator recently developed at the Naval Postgraduate School [Ref. 1]. The flexural disk sensors described in this thesis are used as transducers with a Mach-Zender interferometer used in a push-pull fashion. In response to acceleration, surface strains are induced in optical fibers attached to flexural disks. These strains are interferometrically detected.

Two sensor designs were investigated. The first design attempted to incorporate three significant improvements from a previous accelerometer design at the Naval Postgraduate School (NPS) [Ref. 2]. The desired improvements were: (1) To present elastically restrained boundary conditions; (2) To alleviate coupler cantilever effects believed to be the cause of secondary resonances by tightly housing all interferometer components within the sensor. (3) To use two disks of non-uniform thickness which were milled to both accommodate the attachment of a brass spindle and impose the elastically restrained boundary condition.

The second accelerometer was designed to further investigate the transduction process. Changes from the first design include the removal of the spindle, the use of a single uniform polycarbonate disk with a clamped edge condition and the housing of optical components in a less vulnerable manner.

This thesis presents the theory, design, performance of the two accelerometers, and recommendations to improve fiber-optic accelerometer design.

B. CONVENTIONAL ACCELERATION SENSORS

1. Background

Accelerometers are used in many applications such as shock and vibration measurement in structures and machinery components, long-duration acceleration measurements in vehicles, seismic activity monitoring, navigation, and guidance. Most accelerometers are piezoelectric, piezoresistive, or resistance strain gage types. Although, there has recently been interest in micro-machine accelerometers using semiconductor materials. [Refs. 3: p. 25, 4: pp. 16-1,17-10]

Prior to the discovery and development of piezoelectric ceramics in 1946, wire resistance strain gage sensors were commonly utilized [Ref. 5: p. 2]. Today resistance strain gage accelerometers are less prevalent than other types but are well suited for certain very low frequency applications. Piezoresistive strain gage accelerometers are often used for measurement of low frequency accelerations since their sensitivity is constant at low frequency. The piezoelectric accelerometer is currently the most popular accelerometer for shock and vibration measurement with the advantages of a high resonance frequency, a large usable bandwidth, rugged construction, and good linearity.

2. Conventional Piezoelectric Accelerometers

A conventional seismic accelerometer design has three fundamental components: a hollow case attached to the moving object of interest, a high density mass element, and a sensing element connecting the case and the enclosed mass element. Upon acceleration of the sensor, there exists a relative displacement between the case and mass element. This relative displacement is measured by the sensing element which is typically a piezoelectric ceramic that generates a charge when subjected to strain. The entire sensor design can be represented as a lumped mechanical system as shown in Figure 1.

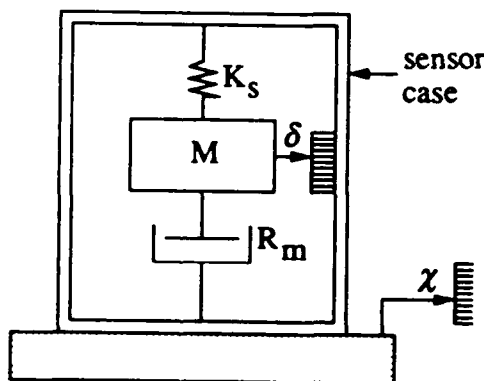


Figure 1. Lumped Parameter Representation of an Accelerometer: A mass element, M , is supported by a spring, K_s , with damping R_m . The sensor is attached to a moving object. δ represents the mass element's displacement relative to the case. χ is the displacement of the moving object and the housing case.

The sensor's equation of motion is

$$M \frac{d^2(\delta - \chi)}{dt^2} + R_m \frac{d(\delta - \chi)}{dt} + K_s(\delta - \chi) = 0, \quad (1.1)$$

where M = mass element, δ = displacement of the mass element relative to the housing case, R_m = mechanical resistance or damping, χ = displacement of the housing case, and K_s = the spring constant. For a sinusoidally varying displacement, the ratio of the relative mass element displacement, δ , to acceleration, $\ddot{\chi}$, of the base can be expressed as [Ref. 6: p. 75]

$$\frac{\delta}{\ddot{\chi}} = \frac{-1}{\omega_n^2} \frac{1}{\sqrt{[1 - (\frac{\omega}{\omega_n})^2]^2 + (\frac{1}{Q} \frac{\omega}{\omega_n})^2}}, \quad (1.2)$$

where the natural or resonance frequency, ω_n , and the quality factor, Q , are defined below. The sharpness of resonance or the quality factor, Q , is 2π times the ratio of the energy stored per cycle to the energy lost per cycle, and is related to the damping factor, ζ , by $Q = \frac{1}{2\zeta}$.

$$Q = \frac{1}{2\zeta} = \frac{\sqrt{K_s M}}{R_m} \quad (1.3)$$

and

$$\omega_n \approx \sqrt{\frac{K_s}{M}} \frac{1}{2Q}. \quad (1.4)$$

For frequencies well below resonance, $\omega \ll \omega_n$,

$$\frac{\delta}{\ddot{\chi}} = -\frac{1}{\omega_n^2}. \quad (1.5)$$

Thus, a constant acceleration sensitivity is obtained over a range of frequencies well below the sensor's resonance frequency. To achieve the largest linear region of constant acceleration sensitivity, the sensor's damping ratio, ζ , is typically adjusted to 0.707 by the addition of oil to the housing cavity. Figure 2 shows the effect various quality factors ($Q = \frac{1}{2\zeta}$) have in equation (1.2). [Refs. 3: pp. 26-37, 4: p. 16-3, 6: p.75, 7: pp.30-32]

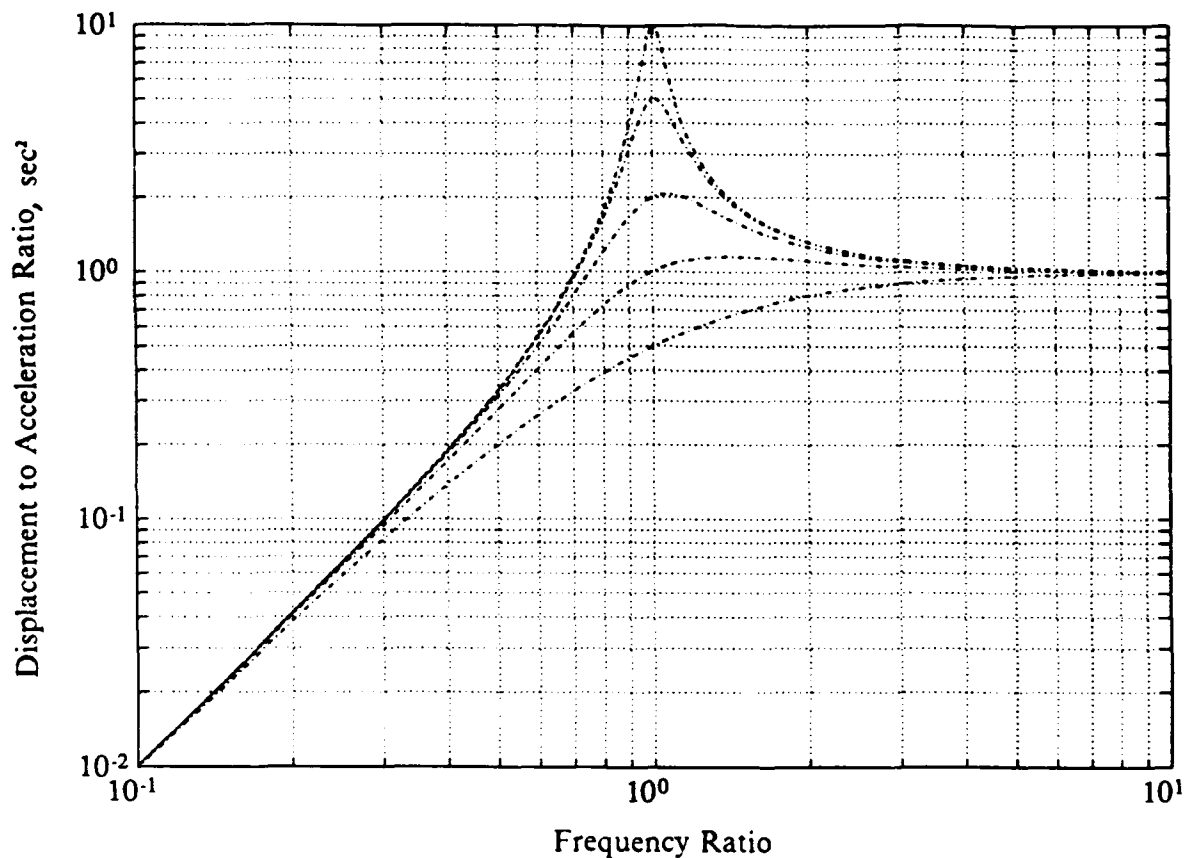


Figure 2. Accelerometer Frequency Response for Different Quality Factors: The ratio of $\frac{\delta}{\gamma}$ for different quality factors is presented versus frequency ratio. The frequency ratio is frequency divided by the resonance frequency. $Q = 10, 5, 2, 1,$ and $0.5,$ for the curves above, with the largest Q having the highest peak.

The sensing element in a piezoelectric seismic sensor can be of compressive or shear design. In both designs, the piezoelectric material experiences a strain during acceleration which can be expressed as [Ref. 4: p. 16-3.]

$$\epsilon = \frac{F}{\kappa}, \quad (1.6)$$

where F is the acceleration induced force and κ is the piezoelectric material's stiffness. In response, a measurable charge, q , appears across the piezoelectric material's internal capacitance. In response,

$$q = A\epsilon, \quad (1.7)$$

where A , having units of coulombs per meter, is a constant determined by the shape, size, and material properties of the sensing element. The force can be expressed as

$$F = M\ddot{\chi}, \quad (1.8)$$

where M is the mass element and $\ddot{\chi}$ is the acceleration. The charge can be expressed as

$$q = \frac{A}{\kappa} M\ddot{\chi}. \quad (1.9)$$

Using equation (1.5), the measurable charge is proportional to δ , the relative displacement of the mass,

$$q \propto \delta. \quad (1.10)$$

3. Conventional Piezoresistive Strain Gage Accelerometers

Piezoresistive strain gage accelerometers have several different designs which rely upon the change in resistance when a piezoresistive material experiences a strain.

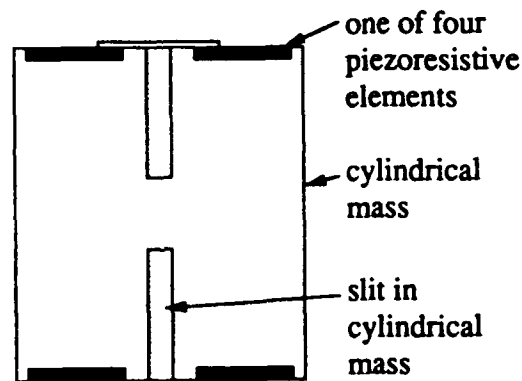


Figure 3. Piezoresistive Strain Gage Accelerometer: A mass element having four identical strips of piezoresistive material attached provides the transduction mechanism.

Figure 3 is a sketch of one piezoresistive strain gage design with four identical strips or elements of piezoresistive material cemented to a cylindrical mass. The four strips are connected using a Wheatstone bridge. A direct current voltage excitation is applied to the Wheatstone bridge input; the output voltage varies with acceleration, as follows: Upward sensor motion causes the upper two piezoresistive elements to increase

in length while the lower two elements decrease in length. For each piezoresistive element, L and R represent the original length and resistance, respectively; ΔL is the element's change in length, and the element's strain is $\varepsilon = \frac{\Delta L}{L}$. The piezoresistive properties of the material caused each length change to be accompanied by a resistance change, ΔR . The gage factor, K , provides the relationship between the fractional change in resistance and the observed strain [Ref. 3: p. 46],

$$K = \frac{\frac{\Delta R}{R}}{\varepsilon} = \frac{\frac{\Delta R}{R}}{\frac{\Delta L}{L}}. \quad (1.11)$$

The piezoresistive sensing elements are positioned in the accelerometer such that the length changes are proportional only to the motion of the mass relative to the case. Thus, the change in resistance is proportional to δ , the relative motion of the mass [Ref. 3: p. 47].

$$\Delta R \propto \delta. \quad (1.12)$$

4. Conventional Strain Gage Accelerometers

A resistance strain gage is a fine wire or very thin foil which exhibits a change in resistance when subjected to strain. Its transduction mechanism is very similar to a piezoresistive accelerometer except for the material used. The basic strain gage accelerometer design has a relatively low sensitivity and is comprised of a mass supported by one or more elastic members to which strain gages are attached. Acceleration of the mass results in strain in the supporting member(s), which, in turn, results in change in the sensing material's gage factor, K . A Wheatstone bridge circuit is typically used to measure the resistance changes.

C. FIBER-OPTIC INTERFEROMETRIC SENSORS

Fiber optic sensors provide means for the mechanical to optical transduction. A measurand disturbs the sensor and causes an intensity, polarization, or phase modulation of the optical signal. In this thesis, the measurand is acceleration and the transducer produces a phase modulation. Several different phase modulated interferometric sensors exist, including Fabry-Perot, Sagnac, Michelson, and Mach-Zender [Ref. 8: p. 491]. Only the Michelson and Mach-Zender configurations will be discussed in this thesis. The reader is referred to [Ref. 9: pp.347-351] for a more complete analysis of other topologies.

A length of optical fiber, L , has a corresponding radian length, ϕ , that can be expressed as [Ref. 10: p. 4],

$$\phi = 2\pi \frac{L}{\frac{\lambda}{n}} = knL, \quad (1.14)$$

where λ is the wavelength of the light traveling within the fiber, n is fiber's index of refraction, and k is the optical wave number, $\frac{2\pi}{\lambda}$.

Changes in the total radian length, or phase, result when a measurand affects the parameters, i.e. [Ref. 11]

$$\Delta\phi = \eta \mathbb{P} k n \Delta L, \quad (1.15)$$

where η is the interferometer configuration parameter accounting for the number of passes of light through the fiber (equalling 1 for a Mach Zender and 2 for a Michelson interferometer) [Ref. 11: p. 43]; \mathbb{P} is a factor compensating for a reduction in sensitivity due to the fiber's photoelastic effect [Ref. 11: p. 49]; k is the wave number; n is the fiber's index of refraction, typically 1.48; and, ΔL is the fiber's change in length. For the fibers used in these experiments, $\mathbb{P} \approx 0.8$.

The relative phase, ϕ , is the parameter which is varied in interferometric sensors. Phase modulations cannot be discerned by photodetectors directly because detectors are not fast enough, but can be converted into intensity modulations using interferometers, but can be converted into intensity change(s) by interferometric techniques. The magnitude of $\Delta\phi$ can be determined by observing the resulting intensity patterns between interfering light waves. Since 1977 [Ref. 10], numerous fiber-optic sensors have been investigated using both the Michelson and Mach-Zender interferometric configurations. [Ref. 10: pp. 5,8]

1. Michelson Fiber-Optic Interferometer

Figure 4 illustrates a Michelson fiber-optic interferometer. The laser provides a coherent light beam which is nominally equally split at a 3 dB (2 x 2) splitter/coupler into two light paths historically called the "reference" and "sensing" legs. A 3 dB coupler ideally directs one half of the light (intensity) through each leg. The "sensing" leg can be attached to a transduction mechanism such as flexural disks or mandrels which respond to a measurand. The end of each fiber leg is cleaved and/or mirrored to provide reflection of light. The reflected light is interferometrically recombined at the coupler.

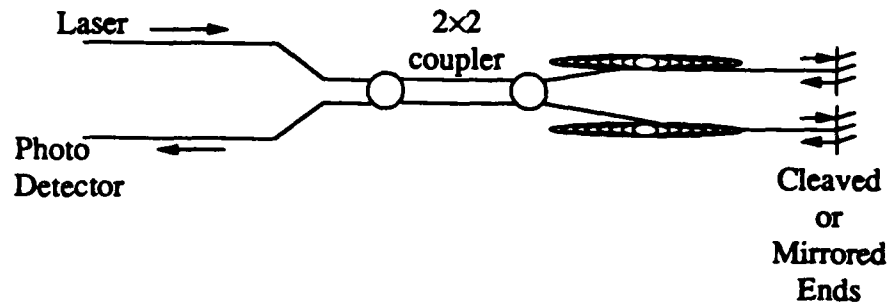


Figure 4. Michelson fiber-optic interferometer: Note the use of cleaved or silvered ends and the requirement for only one coupler. This single coupler is traversed twice by light.

Pedagogically when discussing interferometry, the reference leg is isolated and only one leg is used as a sensor. However, in practice, one typically would rather replace this "reference" leg with a second sensing leg that still preserves detection of the desired signal but also promotes common-mode rejection of unwanted information. Such a sensor is commonly referred to as push-pull.

Light exiting the coupler experiences a phase shift relative to the reference leg when an external measurand acts upon the fiber. Prior to its recombination at the coupler, this "sensing light" is reflected from the cleaved end and again passes through the region of interaction with the measurand. Accordingly, the resultant phase change is twice that of a single pass, as is the case for a Mach-Zender interferometer.

The interferometrically recombined light exits the coupler with intensity fluctuations related to relative change in phase between the sensing leg and the stable reference. These intensity fluctuations are detected at the photodetector where optical energy is converted to electrical energy. The laser also receives the recombined light which, unfortunately, increases noise and modal instability. [Ref. 10: p. 8]

2. Mach-Zender Fiber-Optic Interferometer

Laser light in the fiber is equally split at the 2x2 coupler for propagation in the "reference" and "sensing" legs, and is combined at the second coupler. The relative phase change between the two legs is that phase change experienced by the sensing leg. An advantage of the Mach-Zender configuration is that the laser is subjected to much less

reflected light than in the Michelson configuration, and the photodetector receives more light. In a Mach-Zender both legs may also be used as sensing legs in a push-pull fashion.

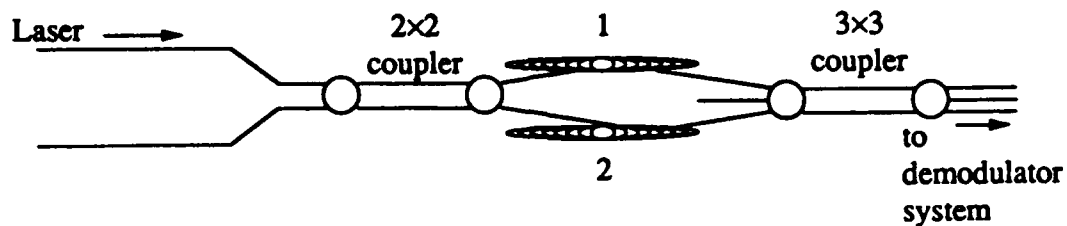


Figure 5. Mach-Zender fiber-optic interferometer: Note the requirement for two separate couplers. Although two 2x2 couplers would accomplish the same interferometry and are more common, a 2x2, 3x3 combination is selected here. One fiber on each of the couplers may be left unused. Effectively, these couplers function as a 1x2, 2x3 combination. In this figure, 1 and 2 identify coils in each of the two interferometer legs.

3. Fiber-Optic Accelerometers

An interferometer becomes a push-pull sensor when the reference leg is replaced by another sensing leg whose phase modulation is 180° out-of-phase compared to the first sensing leg. Since the sensor is configured to measure the acceleration, the relative phase change is doubled in response to acceleration and is forced to zero in response to common mode effects. [Refs. 2: p. 282, 10: p. 7]

One push-pull fiber-optic interferometric accelerometer previously designed and constructed at NPS [Ref. 7], consisted of a seismic mass supported in a case by two rubber mandrels, each wrapped with a single layer of optical fiber. The 10 meter lengths of fiber served as two active legs in a Michelson configuration. Acceleration of the sensor case caused the two rubber mandrels to respond such that one length of fiber elongated while the other shortened in a "push-pull" operation. This design demonstrated a sensitivity of 10,500 radians/g, the highest reported for a fiber-optic

accelerometer to date, and a had resonance frequency of 240 kHz. This accelerometer is referred to as the NPS1 design in the remainder of this thesis.

Tventen et. al. [Ref. 12] constructed another fiber-optic interferometric seismic accelerometer by vertically suspending a seismic mass between two 1.6 cm lengths of tensioned optical fiber. Relative motion between the accelerometer case and the seismic mass caused one fiber to lengthen and the other to shorten. For frequencies below 200 Hz, the observed sensitivity was approximately 2 rad/g. [Refs. 12: pp. 854-856, 7: p.40]

Davis et. al. [Refs. 13] developed a fiber-optic interferometric accelerometer design in which a mercury-filled capsule is the seismic mass. Two 700 m coils of optical fiber are attached to either end of the capsule. This design theoretically would provide a sensitivity of 2,700 rad/g. [Refs. 13: pp. 22-26, 7: p.40]

Another fiber-optic accelerometer previously designed and built at NPS [Refs. 2, 14], is comprised of a cylindrical body with two concentric aluminum disks coupled by an interior spindle. Two flat coils of optical fiber were epoxied to the inner facing disk surfaces and formed a Michelson interferometric leg components. This push-pull configuration had an acceleration sensitivity of 49 rad/g and a resonance frequency of 2.45 kHz. This accelerometer is referred to as the NPS2 design in the remainder of this thesis since it was the second fiber-optic interferometric accelerometer design at the Naval Postgraduate School.

II. MECHANICAL THEORY OF FLEXURAL DISKS

The understanding of an accelerometer's performance is evaluated by predicting and measuring the acceleration sensitivity and the resonance frequency. The resonance frequency is an important sensor characteristic as it determines the maximum bandwidth within which one could expect to observe frequency-independent sensitivities.

The theory of flexural disks is addressed with regard to boundary conditions, strain deformation, resonance frequency and phase modulation induced in optical-fiber adhered to flexural disks. Note that, in general, thin disk theory is applicable for thickness to radius ratios, $\frac{t}{a}$, between 0.001 and 0.05.

A. BOUNDARY CONDITIONS OF THIN DISKS

Knowledge of the boundary condition is essential order to determine how the disk behaves under a particular load and at a particular frequency. The vertical displacement, w ; slope, $\frac{dw}{dr}$; and edge moment, M , are parameters used to describe the boundary condition at an edge. An edge moment is defined for purposes of this thesis as the product of an external vertical force at the edge and a lever arm equal to the radius, a . The neutral surface has zero stress, and typically is the plane which is equal to and parallel to the surfaces, bisecting the thickness of the disk. The central axis is normal to the neutral surface at the center of the disk. Figure 6 is a sketch of a uniform circular disk which shows the neutral surface and central axis.

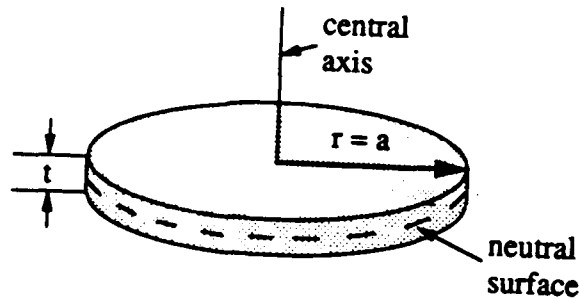


Figure 6. Uniform Circular Disk: The neutral surface is the plane which bisects the disk. The central axis is the normal to the neutral surface at the center of the disk.

1. Simply Supported

At the outer edge of a simply supported disk, the slope is non-zero and there is no displacement. No edge moments are generated since an external vertical force is absent; the edge can rotate about the central axis. The simply supported boundary condition is mathematically expressed as $w = 0$, $\frac{dw}{dr} \neq 0$, and $M = 0$.

2. Clamped

Clamped edges have edge moments which result from the vertical clamping force acting at the outer radii. The clamping force prevents the edge from either displacing or rotating about the central axis. The slope is zero. The clamped boundary condition is mathematically expressed as $w = 0$, $\frac{dw}{dr} = 0$, and $M \neq 0$.

3. Free

A free edge condition is the antithesis of the clamped boundary in that it does have vertical displacement, does allow rotation about the central axis, has a non-zero slope, and does not have edge moments. The free edge is mathematically described by $w \neq 0$, $\frac{dw}{dr} \neq 0$, and $M = 0$.

4. Elastically Restrained

An elastically restrained boundary condition is an intermediate condition which permits finite displacement, rotation about the central axis, and moments; this condition is mathematically expressed by $w \neq 0$, $\frac{dw}{dr} \neq 0$, and $M \neq 0$.

5. Comparisons Between Boundary Conditions

Figure 7 presents the model of a mechanical system comprised of a circular plate supported by two spring stiffnesses, K_r and Ψ . A clamped boundary condition is represented by this model when an infinite stiffness and an infinite ability to prevent rotation are imposed, respectively, by $K_r = \infty$ and $\Psi = \infty$; a free boundary condition is represented by this model when $K_r = 0$ and $\Psi = 0$. Table 1 uses this model to provide comparison of the simply supported, clamped, free, and elastically restrained boundary conditions; this table also compares the mathematical parameters w , $\frac{dw}{dr}$, and M .

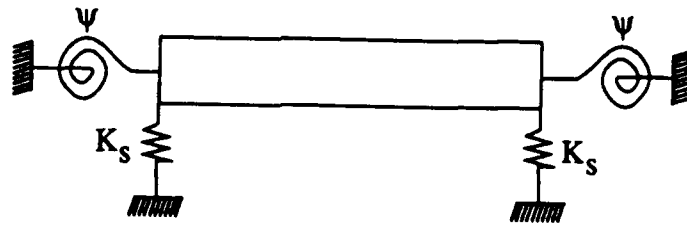


Figure 7. **Elastically Restrained Model:** K_s and Ψ represent the stiffness and torsional stiffness which support the disk, having units of force per unit length squared and moment per unit length.

Table 1. **COMPARISON OF BOUNDARY CONDITIONS:** Boundary conditions are compared with regard to vertical displacement, w ; slope, $\frac{dw}{dr}$; and edge moment, M , at the outer radius, $r = a$; the stiffness and rotational elements of the elastically restrained model, K_s and Ψ , are also compared.

Boundary Condition	w	$\frac{dw}{dr}$	M	K_s	Ψ
Simply Supported	0	finite	0	∞	0
Clamped	0	0	finite	∞	∞
Free	finite	finite	0	0	0
Elastically Restrained	finite	finite	finite	finite	finite

In practice, it is extremely difficult to achieve a single, pure boundary condition. For example, it is virtually impossible to present an infinite amount of stiffness at the outer edge of a purely clamped disk. At best, the existing boundary condition on a given edge is approximated. The easiest boundary condition to achieve is one that is free, however, there are no practical utilizations of this boundary condition in accelerometer design.

The clamped and elastically restrained boundary conditions are germane to this thesis, as are the effects introduced by stepping the disk thickness and by attaching a mass to the disk. The remainder of this thesis will address various topics for the simply supported and clamped boundary conditions; both of these conditions have been rigorously investigated, can be mathematically described with moderate ease, and are peda-

gogically attractive. The effects of a fixed boundary condition, a stepped disk, and a concentrically added mass are difficult to quantify and will be qualitatively presented where appropriate.

B. SURFACE STRAIN DEFORMATION OF THIN DISKS

A force acting on a disk is balanced by a restoring force generated within the disk. This restoring force is manifested by radial and tangential strains or elongations according to Hooke's Law, which is provided below, and is applicable only for elastic deformations which occur below the material yield strength, or the elastic limit [Ref. 15: p.86],

$$\tau = Y\varepsilon, \quad (2.1)$$

where Y is Young's Modulus or the Modulus of Elasticity, τ is stress, and ε is strain or elastic elongation.

When strain conditions are small enough for Hooke's Law to be valid, the following radial and tangential relationships exist and illustrate that stresses are a function of bending moments [Ref. 16: p. 11]:

$$\tau_r = \frac{6M_r}{t^2}, \quad (2.2)$$

$$\tau_t = \frac{6M_t}{t^2}, \quad (2.3)$$

$$\varepsilon_r = \frac{1}{Y} (\tau_r - \sigma\tau_t), \quad (2.4)$$

and

$$\varepsilon_t = \frac{1}{Y} (\tau_t - \sigma\tau_r), \quad (2.5)$$

where subscripts r and t are radial and tangential adjectives respectively, σ is Poisson's ratio, M represents a bending moment, and t is the disk thickness.

Each boundary condition has a unique set of strain equations determined by loading conditions and the associated bending moments; in the following, subscripts "ss" and "cl" represent simply supported and clamped boundary conditions respectively.

1. Simply Supported

For uniform disks with simply supported boundary conditions under uniform pressure, P , it can be shown that the bending moments are [Refs. 16: pp. 55-57, 17: pp. 400,429, 10 : p. 17-19]:

$$M_{r,ss} = \frac{P}{16} (3 + \sigma)(a^2 + r^2) \quad (2.6)$$

and

$$M_{t,ss} = \frac{P}{16} [a^2(3 + \sigma) - r^2(1 + 3\sigma)], \quad (2.7)$$

where a is the disk's outer radius, t is the disk's uniform thickness, and r is the radial distance measured from the center. Using equations (2.1) thru (2.5), the strain equations for the simply supported case are [Refs. 16: pp. 55-57, 17: pp. 400,429, 10 : p. 17-19]:

$$\varepsilon_{r,ss} = \frac{3P(1 - \sigma)(3 + \sigma)}{8Yt^2} \left[a^2 - 3 \frac{(1 + \sigma)}{(3 + \sigma)} r^2 \right] \quad (2.8)$$

and

$$\varepsilon_{t,ss} = \frac{3P(1 - \sigma)(3 + \sigma)}{8Yt^2} \left[a^2 - \frac{(1 + \sigma)}{(3 + \sigma)} r^2 \right]. \quad (2.9)$$

2. Clamped

Similarly, for a uniform disk with clamped boundary conditions under uniform pressure, the bending moment and strain equations are [Refs. 16: pp. 55-57, 17: pp. 400,429, 10 : pp. 17-19]:

$$M_{r,cl} = \frac{P}{16} [a^2(1 + \sigma) - r^2(3 + \sigma)], \quad (2.10)$$

$$M_{t,cl} = \frac{P}{16} [a^2(1 + \sigma) - r^2(1 + 3\sigma)], \quad (2.11)$$

$$\varepsilon_{r,cl} = \frac{3P}{8Yt^2} (1 - \sigma^2)(a^2 - 3r^2), \quad (2.12)$$

and

$$\epsilon_{t,cl} = \frac{3P}{8Yt^2} (1 - \sigma^2)(a^2 - r^2). \quad (2.13)$$

C. RESONANCE FREQUENCY

For any mechanical system, the fundamental resonance frequency, f_0 , is proportional to the ratio of the effective stiffness, k_e , to the effective mass, m_e , [Ref. 18: p. 94],

$$f_0 = \frac{1}{2\pi} \sqrt{\frac{k_e}{m_e}}. \quad (2.14)$$

1. Simply Supported

It can be shown that the resonance frequency for the simply supported uniform disk is [Ref. 18: p. 94],

$$f_{0,ss} = \frac{\Lambda^2 t}{2\pi a^2} \sqrt{\frac{Y}{12(1 - \sigma^2)\rho}}, \quad (2.15)$$

where Λ is the eigenvalue for the Bessel function solution to the Helmholtz equation for transverse vibration in a disk of constant thickness, and is dependent on Poisson's ratio, σ . Table 2 presents several Λ^2 values for the fundamental (0,1) mode and the mode with one radial nodal line (1,1 mode). As noted in Table 2, Λ^2 is very weakly dependent on the Poisson's ratio of the disk material. Λ^2 is also referred to as the resonance frequency parameter. [Ref. 19: pp.9,10]

Table 2. SIMPLY SUPPORTED EIGENVALUES

σ	$\Lambda_{0,1}^2$	$\Lambda_{1,1}^2$
0.250	4.858	
0.300	4.977	13.94
0.333	4.964	

2. Clamped

For the clamped boundary condition, Λ^2 has a value of 10.216 and is independ-

ent of Poisson's ratio since the eigenvalue solution to the Helmholtz equation is not a function of the Poisson's ratio. [Refs. 18: p. 94, 19: p. 9, 10 : p. 21]. The resonance frequency for the clamped uniform disk is given by [Ref. 10: p. 21],

$$f_{0,cl} = \frac{\Lambda^2 t}{2\pi a^2} \sqrt{\frac{Y}{12(1 - \sigma^2)\rho}}. \quad (2.16)$$

3. Disk with Stepped Thickness and/or Added Mass

The literature indicates that several approaches exist to predict the resonance frequency of disks with a stepped thickness and/or a concentrically added mass [Refs. 20, 21, 22, 23 , 24, 25, 26 , 27, 28]. Each method of prediction is complicated, requires significant computer programming to efficiently execute, and almost exclusively is proven for application in very specific situations. However, encouragingly, the cited references all converge towards a common result.

Figure 8 presents four disks of non-uniform thickness and their associated nomenclature. Note that a disk with a stepped central region can effectively be viewed as a disk having a concentrically added mass of similar material. Three methods to predict resonance frequency of non-uniform disks are summarized below in the following.

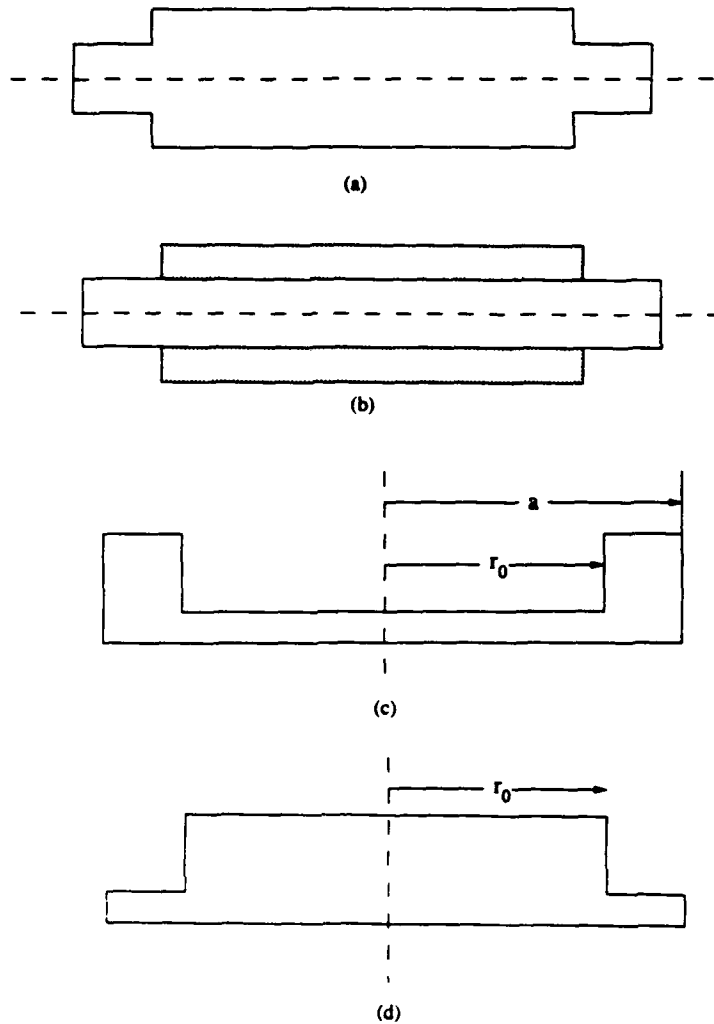


Figure 8. Non-Uniform Circular Disks: (a) Symmetric: the disk is symmetric about the neutral surface, (b) symmetric-added mass: a mass is concentrically added to each surface of the disk such that symmetry about the neutral axis is maintained, (c) axisymmetric outer raised: symmetry about the central axis is maintained with the a larger disk thickness from radii $r = r_0$ to $r = a$, and (d) axisymmetric inner raised: symmetry about the central axis is maintained with a larger disk thickness from $r = 0$ to $r = r_0$.

a. Radius and Mass Ratios Approach

Handelman and Cohen, and C. and S. Huang [Refs. 20, 21] presented findings on clamped symmetric-mass added disks. The mass and radius ratios were

found to be important in determining the resonance frequency. Handelman and Cohen defined γ as the ratio between the *added* density times the *added* thickness, and the disk density times the disk thickness [Ref. 20]; γ is referred to in the literature as the "mass" ratio, although it technically is a ratio in terms of mass per unit area [Refs. 20, 21]. The radius ratio is calculated from the added mass radius and the disk radius.

The resonance frequency is expected to *increase* with increasing radius ratio when γ , the mass ratio, is less than 1.8 or 2.0. In this case, the material added to the disk is effectively increasing the disk stiffness. [Refs. 20: p. 8, 21: p. 223]

For mass ratios, γ , greater than 1.8 or 2.0, the resonance frequency prediction becomes more difficult. At some point, the addition of material to the disk will increase the effective mass instead of the effective stiffness of the disk. A critical radius ratio, α_c , must be determined and compared to the actual radius ratio, and is obtained in two steps: (1) Figure 9 is used to determine the critical mass ratio, γ_c , which corresponds to the actual radius ratio. (2) Figure 10 is used to determine the critical radius ratio, α_c , which corresponds to the critical mass ratio obtained in the previous step. The resonance frequency is expected to *decrease* with increasing radius when the actual radius ratio is less than the critical radius ratio, α_c . Conversely, the resonance frequency is expected to *increase* with increasing radius ratio when the actual radius ratio is greater than the critical radius ratio. [Refs. 20: p. 8, 21: p. 223]

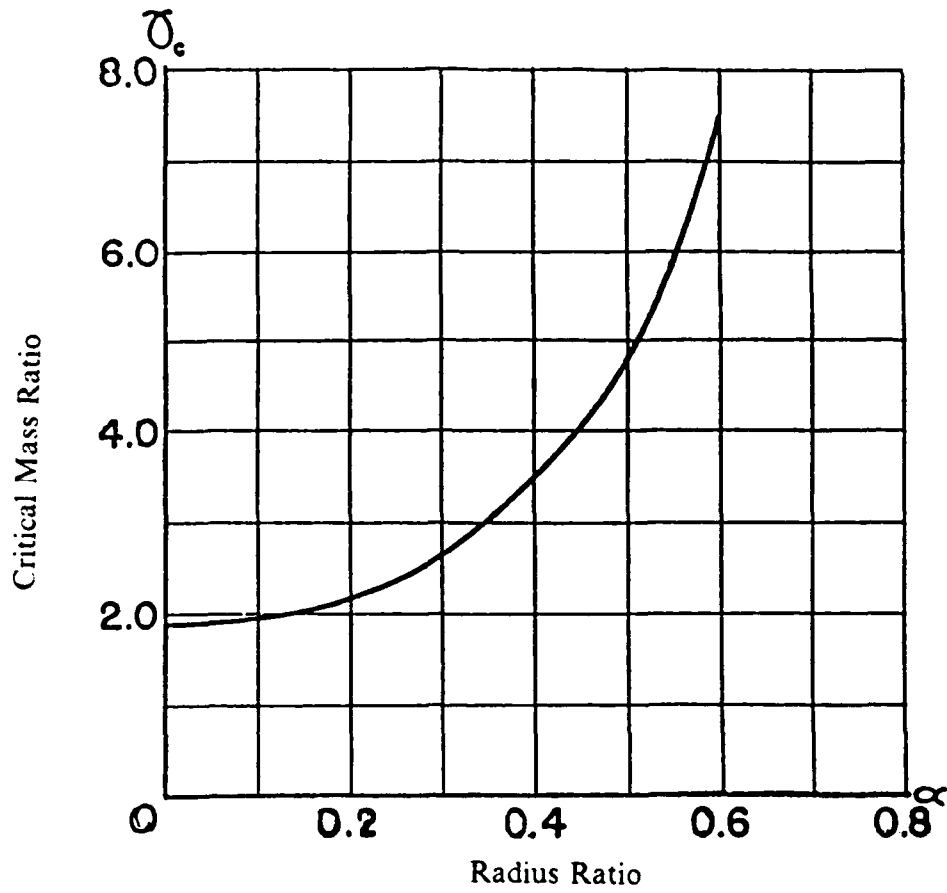


Figure 9. Critical Mass Ratios: Critical mass ratios, γ_c , are plotted versus radius ratios, α . This plot is used to determine a disk's critical mass ratio when its mass ratio, γ , is greater than 1.8. (Adapted from Handelman and Cohen [Ref. 20])

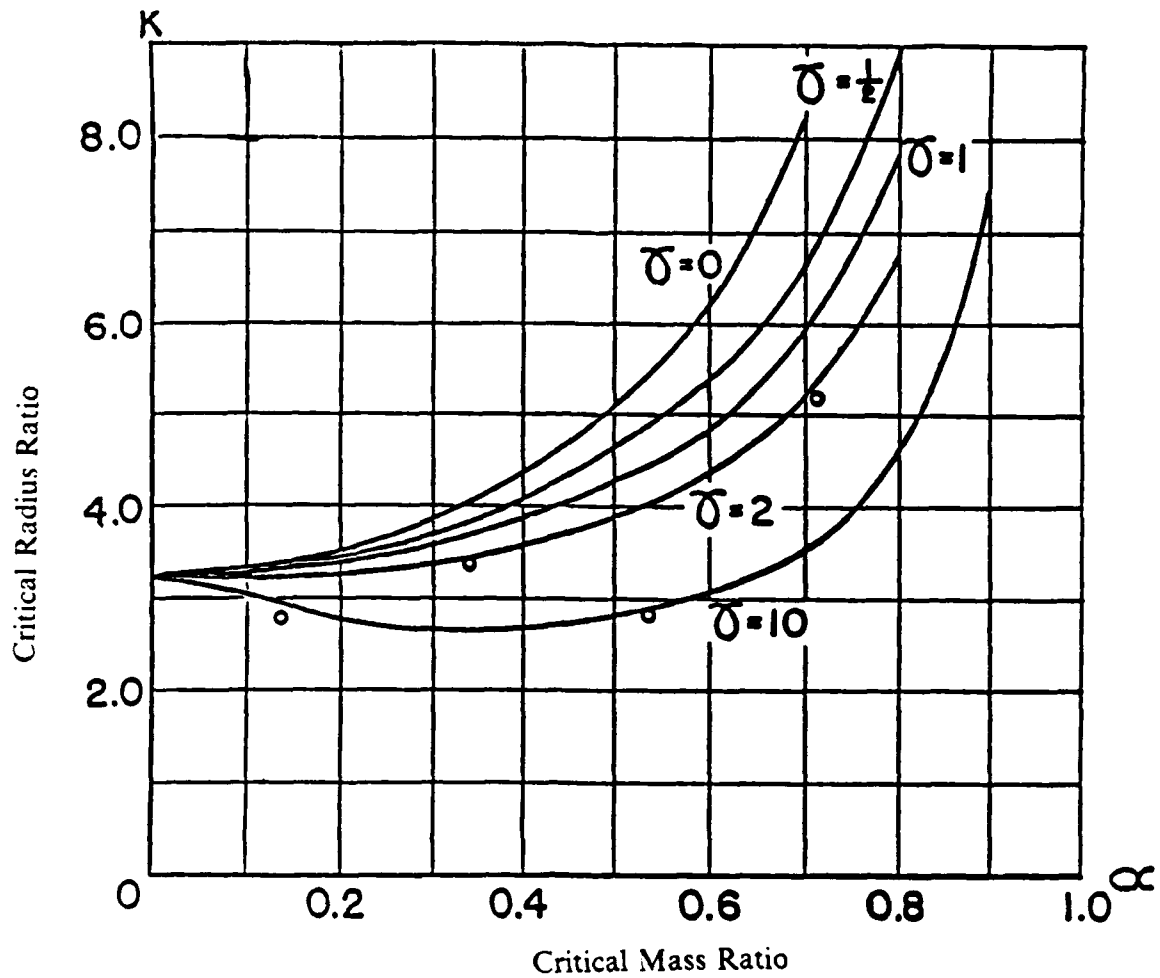


Figure 10. **Critical Radius Ratios:** Critical radius ratios, α_c , are plotted versus critical mass ratios, γ_c . (Adapted from Handelman and Cohen [Ref. 20])

b. Continuity of Zones Approach

Juarez [Ref. 24: p. 411] approached the non-uniform disk by segmenting a free axisymmetric disk into two uniform zones of different thicknesses, as shown in Figure 11. Zone I is a flat plate and Zone II is an annular disk. Classic uniform plate theory provides two equations for the free boundary condition of Zone II. At the common edge, four equations of continuity are available with regard to deflection, slope, shear force, and radial bending moment. The resultant set of six equations is used to numerically solve a complicated frequency equation. Juarez' predicted and observed results are provided in Table 3 for an axisymmetric inner raised disk. [Ref. 24]

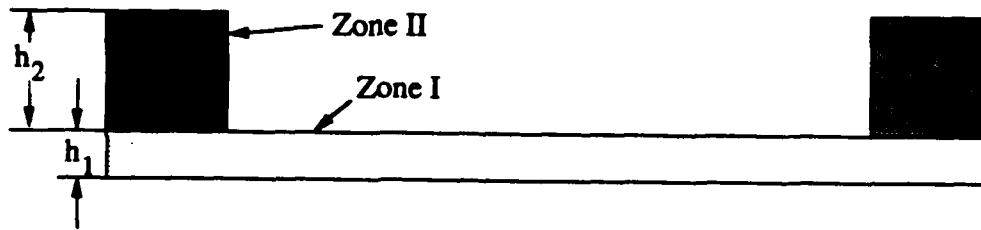


Figure 11. Zones of an Axisymmetric Disk: Zone I is a flat circular disk of thickness h_1 ; Zone II is an annular disk of thickness h_2 .

c. Ritz Method Approach

The Ritz mathematical technique defines a function of one or more indeterminate parameters. The function is minimized with respect to all parameters. The indeterminate parameters are coefficients for simple polynomial expansions which are numerically evaluated. For the circular plate, the function of interest in determining the resonance frequency is the available work, represented by the difference in the maximum kinetic and potential energies.

Laura and Guterrez [Ref. 22: p. 311] investigated symmetric stepped thickness by the Ritz method. The indeterminate parameter was established as a function of the spring and rotational parameters introduced in Figure 7, and the thickness ratio of the stepped and non-stepped regions, $\frac{h_2}{h_1}$. The indeterminate parameter was numerically solved and served as the frequency coefficient for predicting the resonance frequency.

In a similar fashion, Avalos, *et al* [Ref. 25: p. 13] used the Ritz method to generate a frequency equation for axisymmetric disks. Avalos introduced a single exponential Rayleigh parameter which incorporated the dual spring and rotational parameters used by Laura and Guterrez. Table 3 presents the theoretical resonance frequencies predicted by these two Ritz method approaches.

Table 3. STEPPED DISK RESONANCE FREQUENCIES: Predicted and observed resonance frequencies are presented for stepped, aluminum, free-edged disks. Appropriate references are (a) axisymmetric inner-raised (Juarez [Ref. 24: p. 294]), (b) symmetric (Avalos, *et al* [Ref. 25: p. 415]), and (c) symmetric (Laura and Guitierrez [Ref. 27: p. 16]).

Radius Ratio	Theory, Hz (a)	Observed, Hz (a)	Theory, Hz (b)	Theory, Hz (c)
0.0	2622	2560	2621	2622
0.2	2729	2645	2797	3013
0.4	3191	3180	3366	3683
0.6	4020	4130	4129	4264
0.8	4581	4630	4589	4594
1.0	4326	4320	4325	4326

D. PHASE MODULATIONS INDUCED IN OPTICAL-FIBERS

Since the acceleration induced strains in a circular disk are proportional to the pressure induced strains, and the later have been investigated in more detail, the derivation for pressure induced surface strains is presented in this section. The acceleration sensitivity equations are then developed and are used to form useful figures of merit. The theory of modulation and demodulation of Mach-Zender interferometers is also presented.

1. Optical Fiber Strain Induced by Flexural Disk Strain

Consider two separated identical aluminum disks with flat coils of optical-fiber bonded to the two disk surfaces facing each other. Each coil serves as one leg of an interferometer. Strain on the surface of the disk to which the fiber is bonded is presumed to be of equal magnitude and opposite sign. Assuming that the coils of fiber experience the same strains as do their respective disk surfaces, the difference in the fiber strain at any radial distance is,

$$\epsilon(r) = \frac{\Delta \ell(r)}{\ell(r)}, \quad (2.17)$$

where $\Delta \ell(r)$ is the fiber's local change in length, $\ell(r)$ is the fiber's original local length, and $\epsilon(r)$ is the surface strain [Ref. 10: p. 24].

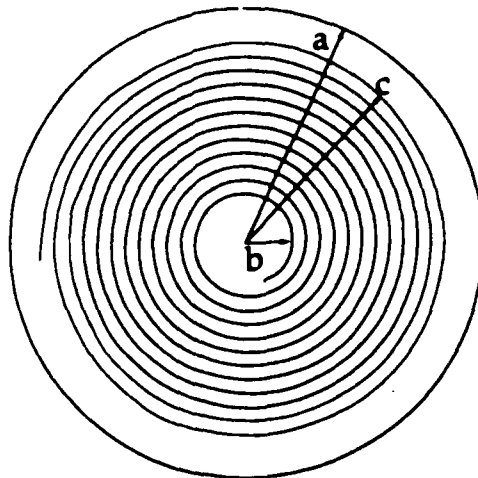


Figure 12. Disk and Fiber Coil Radii: A simple disk and a coil of optical-fiber are shown above with radii indicated: a = outer disk radius, b = coil inner radius, and c = coil outer radius.

Figure 12 is a sketch of a spiral-wound optical-fiber coil bonded to a circular disk. The length of optical-fiber in each coil can be calculated by [Ref. 10: p. 24],

$$L = \int_b^c \frac{2\pi}{D} r dr = \frac{\pi}{D} (c^2 - b^2), \quad (2.18)$$

where D is the fiber's outer diameter, c is the coil's outer radius, and b is the coil's inner radius. The total fiber length difference, ΔL , can be determined by integration of the strain in the length of fiber in one coil, as given by [Ref. 10: p. 24],

$$\Delta L = \int_b^c \Delta \ell(r) dr = \int_b^c \varepsilon(r) \frac{2\pi}{D} r dr. \quad (2.19)$$

Although one might obtain an average strain by dividing ΔL by two lengths of fiber for two legs, historical precedence dictates the division by only one coil length, L [Ref. 10: p. 25]. Most interferometric sensors in the past were not push-pull and thus only one interferometric leg was utilized. The effective strain in the interferometer is [Ref. 10: p. 24],

$$\frac{\Delta L}{L} = \frac{\int_b^c \varepsilon(r) \frac{2\pi}{D} r dr}{\frac{\pi}{D} (c^2 - b^2)}. \quad (2.20)$$

a. Simply Supported Disk

Substituting equation (2.7) into equations (2.19) and (2.20) yields the fiber length change and the effective strain for the simply supported boundary condition [Ref. 10],

$$\Delta L_{ss} = -\frac{P}{Y} \left[\frac{3(1-\sigma)(3+\sigma)}{16t^2} \right] \frac{2\pi}{D} \frac{1}{4} \left\{ 2a^2(c^2 - b^2) - \frac{(1+\sigma)}{(3+\sigma)} (c^2 - b^2) \right\} \quad (2.21)$$

and

$$\frac{\Delta L}{L}_{ss} = -\frac{3(1-\sigma)(5+\sigma)P}{16Yt^2} \left\{ 2a^2 - \frac{(1+\sigma)}{(5+\sigma)} b^2 \right\}. \quad (2.22)$$

b. Clamped Disk

Similarly for the clamped boundary condition, the combination of equations (2.11), (2.19) and (2.20) yields [Ref. 10],

$$\Delta L_{cl} = -\frac{P}{Y} \left[\frac{3(1-\sigma^2)}{16t^2} \right] \frac{\pi}{2D} \{2a^2(c^2 - b^2) - (c^4 - b^4)\} \quad (2.23)$$

and

$$\frac{\Delta L}{L}_{cl} = -\frac{P}{Y} \left[\frac{3(1-\sigma^2)}{16t^2} \right] \{2a^2 - c^2 - b^2\}. \quad (2.24)$$

2. Acceleration Sensitivity

The above equations for the fiber length changes and the effective strains were developed for flexural disks subjected to an external pressure, P , or, for instance, a pressure difference between the inside and outside of the disk, ΔP . However, deflections in the thin disk may alternatively be caused by an acceleration of the sensor. Starting with Newton's Second Law,

$$\Delta P \cdot A = m \Delta a \quad (2.25)$$

where ΔP is a change in pressure, Δa is an acceleration change, and A is the area. For the case of a circular disk of radius a , the mass can be expressed as,

$$m = \rho(\text{Volume}) = \rho t \pi a^2 \quad (2.26)$$

where ρ is the disk's volume density, t is the disk thickness, and πa^2 is the disk's surface area, A . Combination of equations (2.25) and (2.26) results in [Ref. 10],

$$\Delta a = \frac{\Delta P}{\rho t}. \quad (2.27)$$

Recall that the change in radian length for an interferometric sensor is [Ref. 11],

$$\Delta \phi = \eta P k n \Delta L, \quad (2.28)$$

or

$$\Delta \phi = \eta P k n L \frac{\Delta L}{L}. \quad (2.29)$$

The acceleration sensitivity, M_{ac} , is defined as the change in radian length per change in acceleration, and the pressure sensitivity, M_p , is the change in radian length per change in pressure. A simple relationship for the acceleration sensitivity in terms of the pressure sensitivity can be formed by manipulation of equations (2.25) through (2.29) [Ref. 10],

$$M_{ac} = \frac{\Delta\phi}{\Delta a} = \frac{\Delta\phi}{\rho t \Delta a} \rho t = \frac{\Delta\phi}{\Delta P} \rho t, \quad (2.30)$$

$$M_{ac} = \frac{\eta \mathbb{P} k n L \frac{\Delta L}{L}}{\Delta P} \rho t, \quad (2.31)$$

or

$$M_{ac} = \frac{2\pi\eta\mathbb{P}n}{\lambda\Delta P} L\rho t \frac{\Delta L}{L}. \quad (2.32)$$

a. Simply Supported Uniform Disk

Combination of equations (2.18), (2.22), and (2.32) yields the acceleration sensitivity for a simply supported uniform disk [Ref. 10],

$$M_{a,ss} = \frac{2\pi\eta\mathbb{P}n}{\lambda\Delta P} \frac{\pi}{D} (c^2 - b^2)\rho t \left[\frac{-3(1-\sigma)(5+\sigma)P}{16Yt^2} \left\{ 2a^2 - \frac{(1+\sigma)}{(5+\sigma)} b^2 \right\} \right]. \quad (2.33)$$

Notice that the P and ΔP terms are referring to the same change in pressure and thus cancel to simplify the above equation,

$$M_{ac,ss} = \frac{-\pi^2\eta\mathbb{P}\rho}{\lambda D} (c^2 - b^2) \left[\frac{3(1-\sigma)(5+\sigma)}{8Yt} \left\{ 2a^2 - \frac{(1+\sigma)}{(5+\sigma)} b^2 \right\} \right] \quad (2.34)$$

If the length of fiber L is measured and is not algebraically represented, equations (2.22) and (2.32) may alternatively be expressed as [Ref. 10],

$$M_{ac,ss} = \frac{-\pi\eta\mathbb{P}n\rho L}{\lambda} \left[\frac{3(1-\sigma)(5+\sigma)}{8Yt} \left\{ 2a^2 - \frac{(1+\sigma)}{(5+\sigma)} b^2 \right\} \right]. \quad (2.35)$$

b. Clamped Uniform Disk

The acceleration sensitivity for a clamped uniform disk is derived in a similar fashion [Ref. 10]. Combination of equations (2.18), (2.24), and (2.32) yields the acceleration sensitivity for a clamped uniform disk [Ref. 10],

$$M_{ac,cl} = \frac{2\pi\eta\mathbb{P}n}{\lambda\Delta P} \frac{\pi}{D} (c^2 - b^2)\rho l \left[\frac{-3(1-\sigma^2)P}{16Yl^2} \{2a^2 - c^2 - b^2\} \right], \quad (2.36)$$

$$M_{ac,cl} = \frac{-\pi^2\eta\mathbb{P}n\rho}{\lambda D} (c^2 - b^2) \left[\frac{3(1-\sigma^2)}{8Yl} \{2a^2 - c^2 - b^2\} \right], \quad (2.37)$$

or

$$M_{ac,cl} = \frac{-\pi^2\eta\mathbb{P}n\rho}{\lambda D} \left[\frac{3(1-\sigma^2)}{8Yl} \{2a^2(c^2 - b^2) - (c^4 - b^4)\} \right]. \quad (2.38)$$

If the length of fiber, L , is measured and is not algebraically represented, equations (2.24) and (2.32) may alternatively be expressed as [Ref. 10],

$$M_{ac,cl} = \frac{-\pi\eta\mathbb{P}n\rho L}{\lambda} \left[\frac{3(1-\sigma^2)}{8Yl} \{2a^2 - c^2 - b^2\} \right]. \quad (2.39)$$

If the minimum and maximum fiber coil radii are used, $b \ll a$ and $c = a$; then [Ref. 10],

$$M_{ac,cl} = \frac{-\pi^2\eta\mathbb{P}n\rho}{\lambda D} \left[\frac{3(1-\sigma^2)}{8Yl} \right] a^4. \quad (2.40)$$

3. Figures of Merit

A normalized acceleration sensitivity may be obtained by dividing equation (2.40) by the radian length, ϕ . The subscript N indicates a normalized equation. Equations (1.14) and (2.40) reduce to

$$M_{ac,cl,N} = \frac{3\eta\mathbb{P}\rho(1-\sigma^2)a^2}{16Yl}. \quad (2.41)$$

Designing accelerometers involves compromises between sensitivity and bandwidth. The product formed by the normalized sensitivity and the sensor's resonance frequency is *independent of the disk dimensions*, depending only on the physical properties of the disk. This figure of merit permits the designer to trade increased sensitivities for decreased bandwidth, or vice versa. Assuming the fiber coils are wound to the maximum outer radii, i.e $c = a$ and $b \ll a$, the dimension-independent figure of merit for the simply supported boundary condition is determined by equations (1.14), (2.15), and (2.34)

$$M_{ac,ss,N} f_0 = \frac{3\eta\mathbb{P}\Lambda^2}{16\sqrt{12}\pi} \frac{(1-\sigma)(5+\sigma)}{\sqrt{1-\sigma^2}} \sqrt{\frac{\rho}{Y}}, \quad (2.42)$$

and, for the clamped boundary condition, equations (2.16) and (2.41) yield,

$$M_{ac,cl,N} f_0 = \frac{3\eta\mathbb{P}\Lambda^2}{32\sqrt{12}\pi} \sqrt{1-\sigma^2} \sqrt{\frac{\rho}{Y}}. \quad (2.43)$$

$M_{ac,N} f_0$ depends only on the properties of the disk material. Note that a material's speed of sound, v , is defined as $v = \sqrt{\frac{Y}{\rho}}$. Accordingly, the $M_{ac,N} f_0$ figure of merit equations are inversely proportional to the material's speed of sound, v . Table 4 and Table 5 on page 31 present this dimension-independent figure of merit and other figures of merit for the simply supported and clamped boundary conditions.

Table 4. SIMPLY SUPPORTED ACCELEROMETER FIGURES OF MERIT: This table provides figure of merit equations concerning acceleration sensitivity for simply supported flexural disk accelerometer designs, where $c = a$ and $b \ll a$. Here, a is disk radius, t is disk thickness, ρ is volume density, Y is Young's Modulus, and σ is Poisson's ratio; λ is the laser wavelength, D is the fiber outer diameter, Λ^2 is the resonance frequency parameter, n is the fiber's index of refraction, η indicates the number of passes light makes in the interferometer legs, and \mathbb{P} is 0.8, the sensitivity reduction factor due to photostatic effects.

Figure of Merit	Equation for Simply Supported Edges	Attribute
M_{ac}	$\frac{3\pi^2 n \eta \mathbb{P}}{4\lambda D} \frac{a^4}{t} (1-\sigma)(5+\sigma) \frac{\rho}{Y}$	commonly used
$M_{ac,N} = \frac{M_{ac}}{\phi}$	$\frac{3\eta\mathbb{P}}{8} \frac{a^2}{t} (1-\sigma)(5+\sigma) \frac{\rho}{Y}$	normalized to sensor radian length
$M_{ac,N} f_0$	$\frac{3\eta\mathbb{P}\Lambda^2}{16\sqrt{12}\pi} \frac{(1-\sigma)(5+\sigma)}{\sqrt{1-\sigma^2}} \sqrt{\frac{\rho}{Y}}$	dimension-independent
$M_{ac,N} f_0^2$	$\frac{\eta\mathbb{P}\Lambda^4}{128\pi^2} \frac{t}{a^2} \frac{(1-\sigma)(5+\sigma)}{(1-\sigma^2)}$	analog to pressure's dimension independent figure of merit

Table 5. CLAMPED ACCELEROMETER FIGURES OF MERIT: This table provides figures of merit equations concerning acceleration sensitivity for clamped flexural disk accelerometer designs, where $c = a$ and $b \ll a$. Here, a is disk radius, t is disk thickness, ρ is volume density, Y is Young's Modulus, and σ is Poisson's ratio; λ is the laser wavelength, D is the fiber outer diameter, Λ^2 is the resonance frequency parameter, n is the fiber's index of refraction, η indicates the number of passes light makes in the interferometer legs, and \mathbb{P} is 0.8, the sensitivity reduction factor due to photostatic effects.

Figure of Merit	Equation for Clamped Edges	Attribute
M_{ac}	$\frac{3\pi^2 n \eta \mathbb{P}}{8\lambda D} \frac{a^4}{t} (1 - \sigma^2) \frac{\rho}{Y}$	commonly used
$M_{ac, Y}$	$\frac{3\eta \mathbb{P} (1 - \sigma^2)}{16} \frac{a^2}{t} \frac{\rho}{Y}$	normalized to sensor radian length
M_{ac, N, f_0}	$\frac{3\eta \mathbb{P} \Lambda^2}{32 \sqrt{12} \pi} \sqrt{1 - \sigma^2} \sqrt{\frac{\rho}{Y}}$	dimension-independent
M_{ac, N, f_0^2}	$\frac{\eta \mathbb{P} \Lambda^4}{256\pi^2} \frac{t}{a^2}$	analog to pressure's dimension independent figure of merit

The acceleration and pressure sensitivities are related by equation (2.30), such that

$$\frac{M_{ac}}{M_p} = \rho t. \quad (2.44)$$

For demonstrative purposes, the dimension-independent figure of merit for pressure sensitivities is presented only for the clamped boundary condition. The pressure sensitivity for the clamped boundary condition, when $b \ll a$ and $c = a$, is

$$M_{clp} = \frac{\Delta\phi}{\Delta P} = \frac{2\pi\eta\mathbb{P}n}{\lambda} \frac{\pi}{D} \frac{3(1 - \sigma^2)}{16Yt^2} a^4. \quad (2.45)$$

Equations (2.16) and (2.45) yield,

$$M_{p,cl} f_0^2 = \frac{n\eta\mathbb{P}}{128} \frac{\Lambda^4}{\lambda D} \frac{1}{\rho}, \quad (2.46)$$

which is the dimension-independent figure of merit for pressure sensitivity. M, f_0^2 depends only on the properties of the disk material and the type of optical fiber used.

Table 6 uses the dimension-independent figure of merit equations, equations (2.41) and (2.46), to demonstrate the expected sensitivity improvements realized by using some disk materials other than aluminum. When compared to aluminum, a polycarbonate material will improve accelerometer and hydrophone sensitivities by factors of approximately 13 and 28 respectively, but will reduce resonance frequencies by approximately 0.75.

Once the disk material has been selected, the figure of merit equations can be used to determine disk radii corresponding to various sensitivities and bandwidths. For example, equation (2.43) can be conveniently altered to consider compromises for an accelerometer design with clamped edges, such that

$$M_{ac,N} f_0 = \frac{1}{\phi} \frac{\Delta\phi}{\Delta a} f_0 = \frac{3\eta\mathbb{P}\Lambda^2}{32\pi} \sqrt{\frac{(1-\sigma^2)}{12}} \frac{1}{v}, \quad (2.47)$$

where

$$\phi = \frac{2\pi nL}{\lambda} = \frac{2\pi^2 n a^2}{\lambda D}. \quad (2.48)$$

Manipulation of equations (2.47) and (2.48) yields

$$M_{ac} = \frac{\pi\eta\mathbb{P}n}{\lambda D} \frac{3\Lambda^2}{16} \sqrt{\frac{(1-\sigma^2)}{12}} \frac{a^2}{v f_0}, \quad (2.49)$$

$$a^2 = \frac{1}{\eta\mathbb{P}} \frac{M_{ac} v f_0}{\left[\frac{\pi n}{\lambda D} \frac{3\Lambda^2}{16} \sqrt{\frac{(1-\sigma^2)}{12}} \right]}. \quad (2.50)$$

In this example, assume $n = 1.48$, $\lambda = 830\text{nm}$, $D = 250\mu\text{m}$, and $\Lambda^2 = 10.216$. Equation (2.50) becomes

$$a^2 = (8.07 \times 10^{-11}) \frac{M_{ac} v f_0}{\sqrt{(1-\sigma^2)}} \quad (2.51)$$

Table 7, Table 8, and Table 9 utilize equation (2.51) to demonstrate the *general* compromises between acceleration sensitivity and bandwidth when different radii are considered in designs using polycarbonate, Lucite, and aluminum.

Table 6. SENSITIVITY COMPARISONS: This table shows acceleration and pressure sensitivity improvements when compared to sensors built using clamped aluminum disks. Material properties obtained from [Ref. 18: p. 461], except for *Stycast*[®] 1266, obtained from [Ref. 29: p. 33], and polycarbonate, obtained from [Ref. 30].

Material	ν (m/sec) Sound Speed	$\frac{M_{ac}}{M_{ac, ALUMINUM}}$	Y (GPa) Modulus	$\frac{M_p}{M_{p, ALUMINUM}}$
Aluminum	5150	1.0	71.0	1.0
Glass	5200	1.0	60.2	1.2
Copper	3700	1.9	122.0	0.6
Lucite	1800	8.2	4.0	17.8
Hard Rubber	1450	12.6	2.30	30.9
<i>Stycast</i> [®] 1266	1506	11.7	2.7	26.3
Polycarbonate	1447	12.7	2.49	28.5
Lead	1200	18.4	10.65	6.7

Table 7. COMPARISON OF POLYCARBONATE DISKS: The compromises between acceleration sensitivity and bandwidth are presented. M_{ac} (rad/g), is provided for various radius and frequency combinations. $v = 1447m/s$ and $\sigma = 0.347$ [Ref. 30].

a, cm	2500 Hz	1800 Hz	1250 Hz	500 Hz
10.8	40.0	55.5	79.9	199.7
4.0	5.5	7.6	10.9	27.4
3.2	3.5	4.9	7.0	17.5
3.0	3.0	4.3	6.1	15.4
2.5	2.1	2.9	4.3	10.7
2.0	1.4	1.9	2.7	6.8

Table 8. COMPARISON OF LUCITE DISKS: The compromises between acceleration sensitivity and bandwidth are presented. M_{ac} (rad/g), is provided for various radius and frequency combinations. $v = 1800m/s$ and $\sigma = 0.4$ [Ref. 18].

a, cm	2500 Hz	1800 Hz	1250 Hz	500 Hz
12.6	39.1	54.3	78.2	195.6
4.0	3.9	5.5	7.9	19.7
3.2	2.5	3.5	5.1	12.6
3.0	2.2	3.1	4.4	11.1
2.5	1.5	2.1	3.1	7.7
2.0	0.9	1.4	1.9	4.9

Table 9. COMPARISON OF ALUMINUM DISKS: The compromises between acceleration sensitivity and bandwidth are observed. M_{ac} (rad/g), is provided for various radius and frequency combinations. $v = 5150m/s$ and $\sigma = 0.33$ [Ref. 18].

a, cm	2500 Hz	1800 Hz	1250 Hz	500 Hz
21.0	39.2	54.4	78.3	195.8
4.0	1.4	1.9	2.8	7.1
3.2	0.91	1.3	1.8	4.5
3.0	0.79	1.1	1.6	3.9
2.5	0.56	0.77	1.1	2.8
2.0	0.36	0.49	0.71	1.7

4. Phase Modulation and Demodulation of Mach-Zender Interferometers

a. Phase Modulated Intensities with a 3 x 3 Coupler

Consider a Mach-Zender interferometer as shown in Figure 5. Laser light is injected into the 2x2 coupler and divided between the two fibers forming the legs of the interferometer. The measurand of interest induces an optical path length difference between the two legs. An electric field component is associated with the light intensity of each leg; ideally, these field components are of equal magnitude.

E_1 and E_2 represent the electric field vectors and combine as shown in Figure 13. Depending of the net phase and amplitude difference between the two vectors, the resultant vector can range from a minimum of zero to a maximum of the square of the vector addition of the two electric field components. The resultant vector is also representative of the modulated output intensities detected at each output of the 3x3 coupler, as follows:

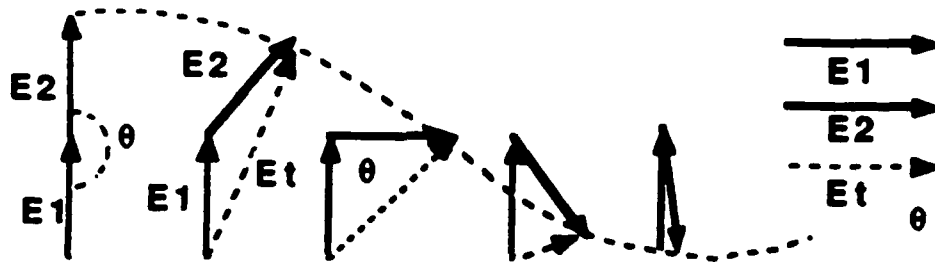


Figure 13. Illustration of Interfering Electric Field Vectors: Electric field vectors E_1 and E_2 are of equal magnitude and have a time varying phase difference $180^\circ - \theta(t)$, as in push-pull sensors.

The light intensity at each 3x3 output leg can be expressed as

$$i_k(t) = C + B \cos[\Delta\phi(t) + \phi(t)_{st} - (k - 1) \frac{2\pi}{3}], \quad (2.52)$$

where i_k is the intensity of the k^{th} leg, C is the central intensity from all three legs and B is the peak change in intensity from the central value [Refs. 31, 1]. $\Delta\phi(t)$ is the phase change associated with strains induced in the optical-fiber. $\phi(t)_{st}$ is the static phase term which accounts for noise contributions. Figure 14 presents the theoretical phase modulated intensities expected from each 3x3 leg for $\Delta\phi(t) = A \sin(\omega t)$; note that each signal is 120° out of phase.

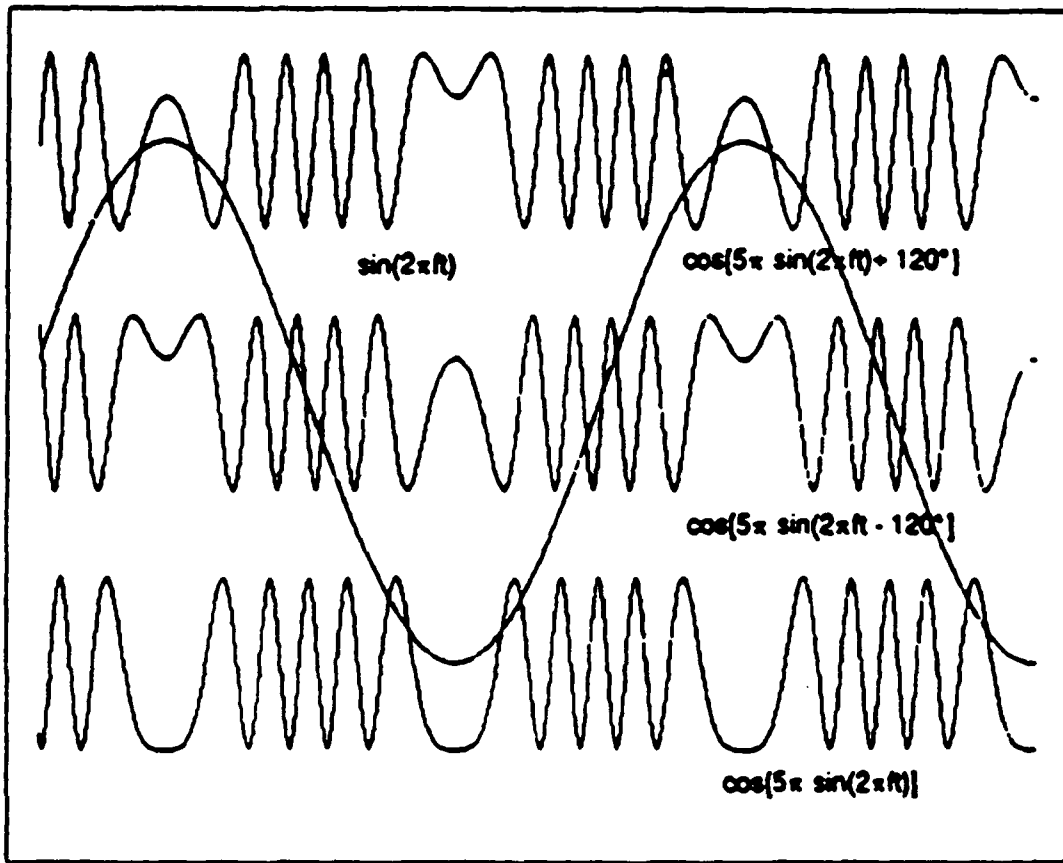


Figure 14. **Theoretical 3x3 Phase Modulated Intensities:** Theoretical intensities for each 3x3 output leg for are illustrated with a stimulus of $\Delta\phi(t) = 5\pi \sin(\omega t)$ superimposed. (Adapted from Cameron [Ref. 32])

The induced phase modulation can be determined by examining the interferometric output and counting the number of fringes. One fringe equates to 2π radians of phase modulation. In Figure 14, five peak to peak fringes are present in one half-cycle of the stimulus; the amplitude of the phase shift is therefore $5\left(\frac{2\pi}{2}\right) = 15.7$ radians.

b. Symmetric 3x3 Coupler Based Demodulator

A symmetric demodulator was recently designed and built at the Naval Postgraduate School which recovers the signal of interest from the output of a 3x3 coupler in a Mach-Zender interferometer [Ref. 31, 1, 32]. The time varying light intensities from each leg are processed to provide a signal that is proportional to the phase

modulation. Figure 15 is a block diagram of the symmetric demodulator. A summary of the algorithm development follows.

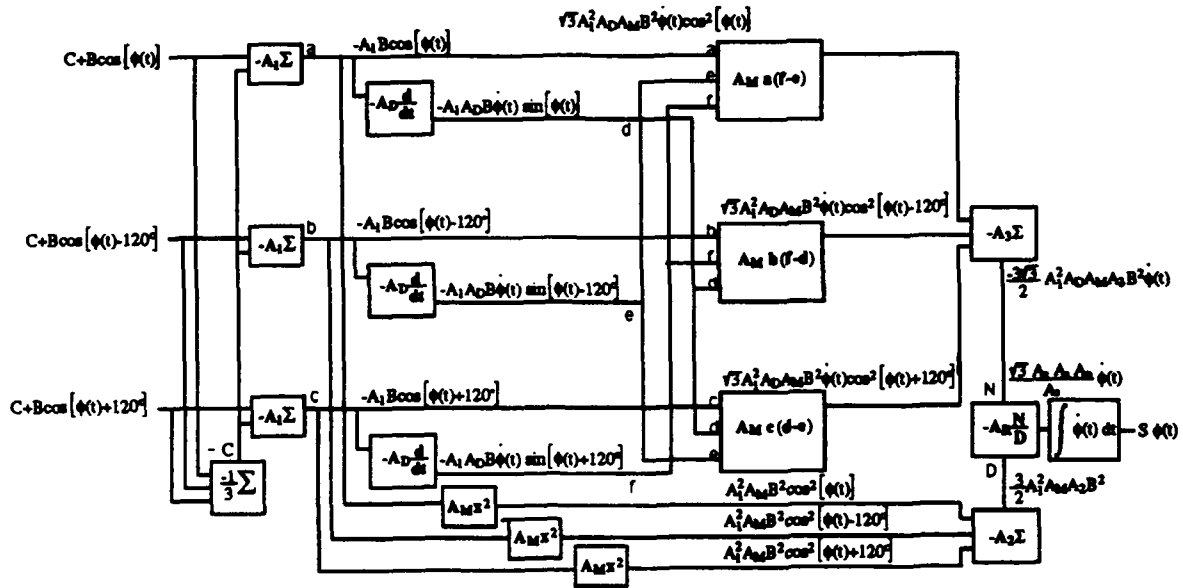


Figure 15. Algorithm for the Symmetric Demodulator. (Adapted from Cameron, modified by Gardner [Ref. 32])

The phase modulated intensity in each 3x3 output leg is given by equation (2.52), repeated here for convenience, for the three legs, $k = 1$ thru 3 [Refs. 1, 32],

$$i_k(t) = C + B \cos\left[\Delta\phi(t) + \phi(t)_{st} - (k - 1) \frac{2\pi}{3}\right], \quad (2.52)$$

Letting the instantaneous phase difference between the two legs be

$$\phi(t) = \Delta\phi(t) + \phi(t)_{st}, \quad (2.53)$$

such that

$$i_k(t) = C + B \cos\left[\phi(t) - (k-1)\frac{2\pi}{3}\right]. \quad (2.54)$$

To eliminate fluctuations in the central intensity term, C is isolated. The intensities from each leg are added with an inverting adder of gain $-\frac{1}{3}$; the result of this summation is $-C$ [Refs. 1, 32],

$$\sum_{k=1}^3 \left(-\frac{1}{3}\right) i_k(t) = -C. \quad (2.55)$$

The above result is added to each signal with an adder of gain A_1 ; the resultant signal is [Refs. 1, 32],

$$x_k(t) = A_1 B \cos\left[\phi(t) - (k-1)\frac{2\pi}{3}\right]. \quad (2.56)$$

Differentiation is now accomplished with a gain A_D to extract the derivative of $\phi(t)$, resulting in [Refs. 1, 32],

$$\dot{x}_k(t) = -A_1 A_D B \dot{\phi}(t) \sin\left[\phi(t) - (k-1)\frac{2\pi}{3}\right]. \quad (2.57)$$

To remove the sinusoidal dependence of $x_k(t)$, each signal is first multiplied by the difference of the remaining signals' derivatives; this is accomplished with a multiplier gain of A_M and an adder gain of A_1 . It is convenient to apply the trigometric identity,

$$\sin(\alpha + \beta) - \sin(\alpha - \beta) = 2 \cos(\alpha) \sin(\beta), \quad (2.58)$$

to obtain [Refs. 1, 32],

$$A_M x_1 (\dot{x}_2 - \dot{x}_3) = \sqrt{3} A_M A_1^2 A_D B^2 \dot{\phi} \cos^2(\phi(t) - 0), \quad (2.59)$$

$$A_M x_2 (\dot{x}_3 - \dot{x}_1) = \sqrt{3} A_M A_1^2 A_D B^2 \dot{\phi} \cos^2\left(\phi(t) - \frac{2\pi}{3}\right), \quad (2.60)$$

and

$$A_M x_3 (\dot{x}_1 - \dot{x}_2) = \sqrt{3} A_M A_1^2 A_D B^2 \dot{\phi} \cos^2\left(\phi(t) + \frac{2\pi}{3}\right). \quad (2.61)$$

Equations (2.59), (2.60), and (2.61) are combined with an adder of gain A_3 to yield [Refs. 1, 32],

$$\sqrt{3} A_3 A_M A_1^2 A_D B^2 \dot{\phi}(t) \left[\cos^2(\phi(t)) + \cos^2\left(\phi(t) - \frac{2\pi}{3}\right) + \cos^2\left(\phi(t) + \frac{2\pi}{3}\right) \right]. \quad (2.62)$$

By application of the following identity for $N = 3$

$$\sum_{k=0}^{N-1} \cos^2\left(\phi(t) + \frac{k 2\pi}{N}\right) = \frac{N}{2}. \quad (2.63)$$

Equation (2.62) simplifies to [Refs. 1, 32],

$$\frac{3}{2} \sqrt{3} A_3 A_M A_1^2 A_D B^2 \dot{\phi}, \quad (2.64)$$

For any phase difference, equation (2.64) shows that

$$\cos^2(\phi + 0) + \cos^2\left(\phi + \frac{2\pi}{3}\right) + \cos^2\left(\phi + \frac{4\pi}{3}\right) = \frac{3}{2}. \quad (2.63)$$

The B^2 term can be obtained by adding the square of each scaled signal $x_i(t)$. Equation (2.63) and multiplier gains A_M and A_2 produce [Refs. 1, 32],

$$A_2 \sum_{k=1}^{N-1} A_M \left\{ A_1 B \cos\left[\phi(t) - (k-1) \frac{2\pi}{N}\right] \right\}^2 = \frac{3}{2} A_2 A_M A_1^2 B^2. \quad (2.66)$$

B^2 is a common term in both of the previous equations. Division of equation (2.63) by equation (2.66) with a divider of gain A_d yields the scaled time derivative of the phase modulation [Refs. 1, 32],

$$A_d \frac{\frac{3}{2} \sqrt{3} A_3 A_M A_1^2 A_D B^2 \dot{\phi}(t)}{\frac{3}{2} A_2 A_M A_1^2 B^2} = \frac{\sqrt{3} A_3 A_D A_d}{A_2} \dot{\phi}(t). \quad (2.67)$$

The scaled phase modulation is obtained by *integration* of the previous equation with an integrator of gain A_1 [Ref. 31, 1, 32], producing

$$\frac{\sqrt{3} A_1 A_3 A_D A_d}{A_2} \phi(t). \quad (2.68)$$

Accordingly, the symmetric demodulator's output signal is proportional to the phase modulation $\phi(t)$ caused by the measurand. The gains selected for the circuit elements determine the scaling factor, which, for the demodulator implementation considered in this thesis, was 31 mv/rad. A second and simpler demodulator implementation had a scale factor of 87 ± 1 mv/rad.

III. SENSOR DESIGN, CONSTRUCTION, AND PERFORMANCE

Two very similar accelerometer designs are investigated in this thesis. In this chapter, the design, construction, testing, and performance are presented.

A. SENSOR DESIGN

Both sensors use the Mach-Zender interferometric configuration and are comprised of flexural disks mounted to a hollowed base which houses a 2x2 coupler, a 3x3 coupler, splice protectors, and excess fiber. The disks and base are joined by six screws near the sensor's outer radius. The base has one side port to provide access for one input fiber and three output fibers. Figure 16 and Figure 18 provide cross-sectional views of the accelerometers. Table 10 presents the optical components used in both designs; Table 11 presents a summary of material properties for both designs.

1. Dual Aluminum Disk (NPS3) Design

In the first design of this thesis, two stepped flexural disks are made from 6061-T6 aluminum stock with inner and outer diameters of 7.4 cm and 6.2 cm respectively. The disk is stepped by the placement of a thin groove to create an elastically restrained edge, and by the placement of a small raised ring in the center to provide for the concentric attachment of a brass spindle between the two disks. The predominant disk thickness is 1.5 mm. Note that this design shall be referred to as the NPS3 design in the remainder of this thesis, as it is the third fiber-optic accelerometer built at the Naval Postgraduate School. Figure 17 is a cross-sectional view of the aluminum disks.

The disk's stepped features preclude confident predictions of resonance frequency and acceleration sensitivity. Limits of the sensor's resonance frequency can be obtained from the equations for simply supported and clamped boundary conditions, i.e. between 2.07 kHz and 4.25 kHz. The raised small diameter on each disk adds mass such that the mass ratio, γ , is < 0.1 ; since $\gamma < 1.8$, it is not necessary to determine the critical radius ratio; the resonance frequency is expected to increase with increasing radius. For the simply supported case, this resonance should be > 2.07 kHz, and for the clamped case, > 4.25 kHz [Ref. 20].

With the two disks and spindle joined together, one half of the brass spindle mass is added to each disk, yielding mass and radius ratios, $\gamma = 0.2$ and $\alpha = 0.4$, respectively. Since the mass ratio, γ , is not greater than 1.8, the resonance frequency is ex-

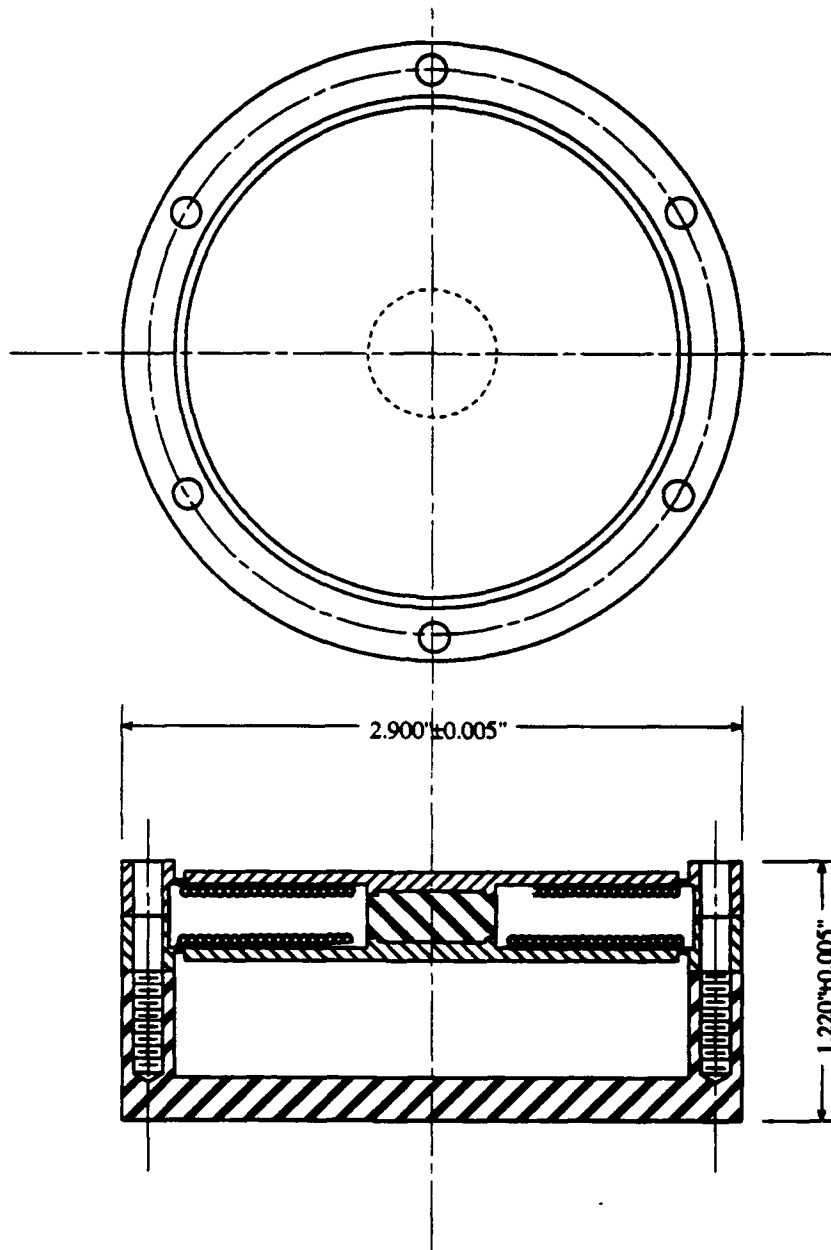


Figure 16. Cross-sectional View of the Dual Aluminum Disk Design: This design is referred to as the NPS3 design.

pected to increase as the radius of the added mass increases, and it is not necessary to determine the critical mass ratio. [Ref. 20]

To predict the resonance of the sensor, one must consider the mass added to the disks by the optical fiber coils and epoxy. It is estimated that the fiber coils and epoxy increased the mass ratio to $\gamma = 0.7$. Accordingly, the resonance frequency is expected to increase with increasing radius, since $\gamma < 1.8$. [Ref. 20]

This attempted application of the radius and mass ratios approach to better predict the resonance frequency is not entirely valid. The stepped thicknesses caused by the thin groove at the disk edge, the ring at the center, the potentially non-rigid attachment of the spindle, and the four small fiber path holes are not precisely treated in the prediction. The best prediction is that the sensor's resonance frequency should be greater than 2.08 kHz.

Equations (2.38) and (2.34) predict acceleration sensitivities of 0.4 and 2.7 rad/g, for clamped and simply supported edge conditions, respectively.

2. Polycarbonate Disk (NPS4) Design

The second accelerometer design in this thesis uses one 6.2 cm diameter polycarbonate disk of uniform 1.0 mm thickness with a clamped edge condition. This design shall be referred to as the NPS4 design in the remainder of this thesis.

The resonance frequency is predicted to be 753.6 Hz for a clamped edge condition. For the simply supported boundary condition, the resonance frequency parameter, Λ^2 , is very weakly dependent on the Poisson's ratio, σ in equation (2.15). The Poisson's ratio for polycarbonate is 0.347 [Ref. 30]. Since a Λ^2 value was not available for $\sigma = 0.347$, a Λ^2 value for $\sigma = 0.33$ is used to predict a simply supported resonance frequency of 366.2 Hz. The ratio of the mass added by the fiber coils and epoxy to disk mass is 0.7. Since $\gamma < 1.8$, it was not necessary to determine the critical radius ratio; the resonance frequency is expected to increase. The sensor's resonance frequency should be >367 for the simply supported case, and >753 Hz for the clamped case. Note that this prediction does not consider the effect of the two small (1.0 mm) diameter holes drilled at the disk edge.

Equations (2.38) and (2.34) predict acceleration sensitivities between 7.3 and 54.0 rad/g, for the clamped and simply supported edge conditions, respectively.

B. SENSOR CONSTRUCTION

Figure 19 illustrates a winding jig used to wind optical fiber into flat coils. Two acrylic disks are separated by a washer of sufficient thickness to permit a single layer of

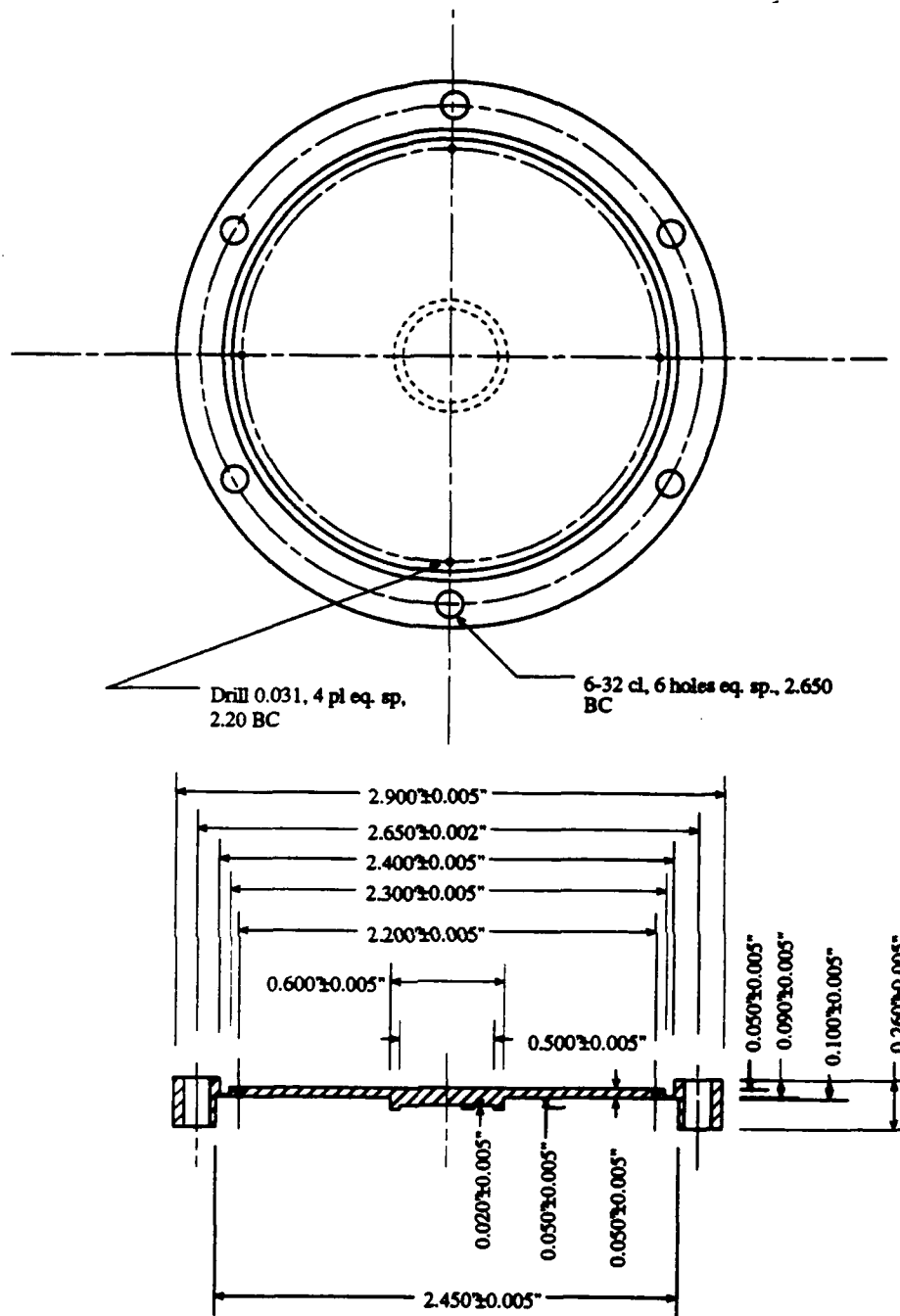


Figure 17. Illustration of the Top and Bottom Aluminum Disks, NPS3
Design: When assembled, the stepped section clamping the brass spindle fare each other. The top disk did not have the two 0.031 inch holes.

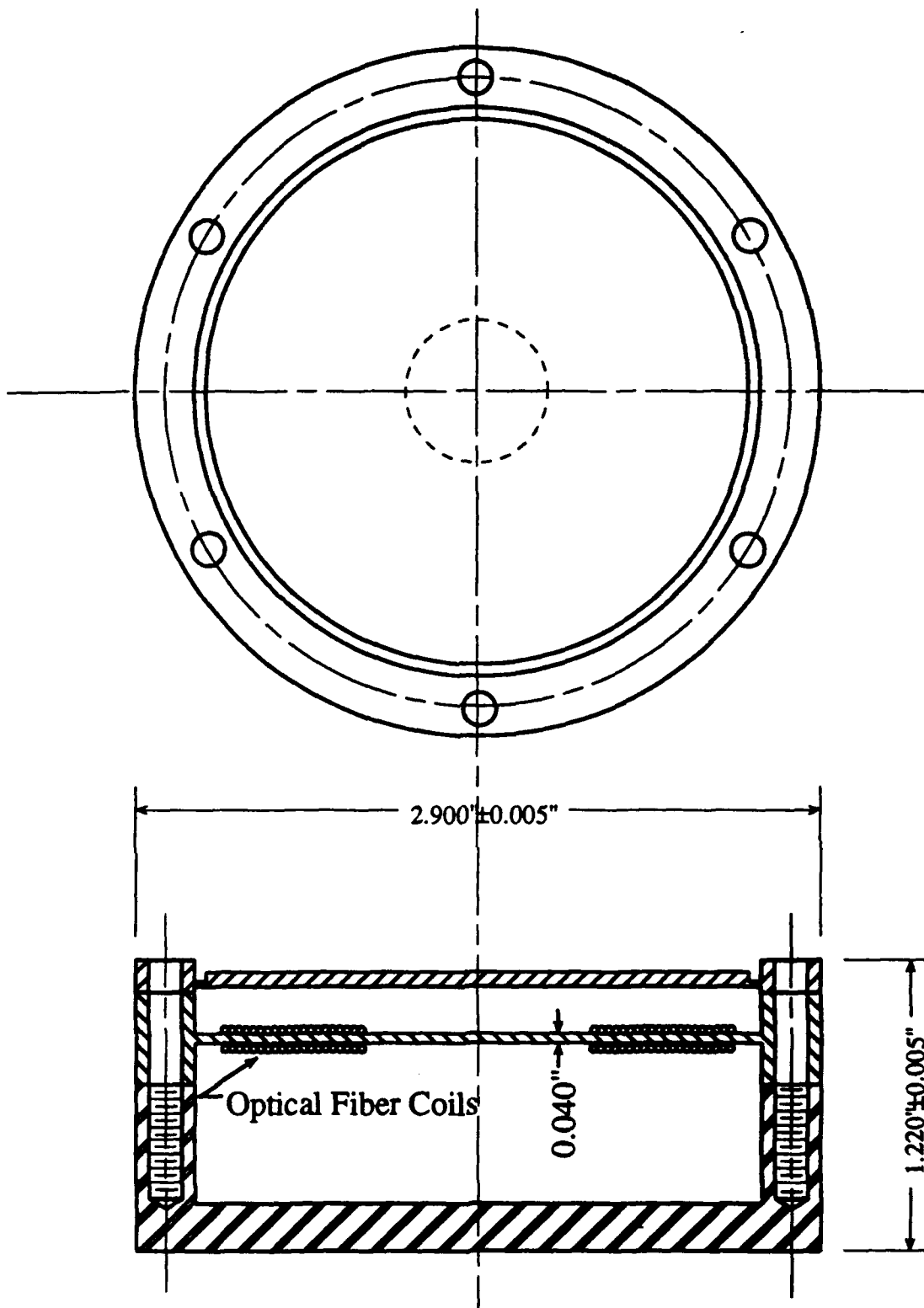


Figure 18. Cross-sectional View of the Polycarbonate Disk Design: This design is referred to as the NPS4 design.

optical fiber to be tightly wound between the acrylic disks. Rubber cement was applied to the coil through the four openings on the top acrylic disk to keep the coils in their spiral state. The coils were removed and epoxied to the disk surfaces.

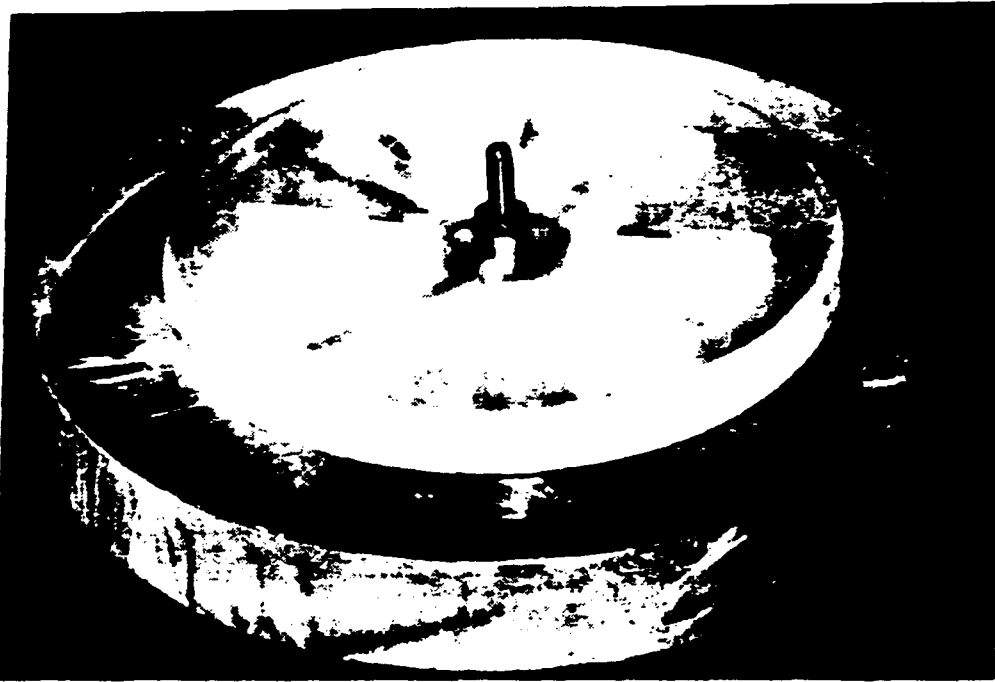


Figure 19. Coil Winding Jig: Apparatus used to wind flat coils of optical fiber [Ref. 10: p.41].

Sensor assembly begins with the fabrication of a Mach-Zender interferometer as shown in Figure 5, and is completed with the packaging of all sensor components. Appendix A presents the details of the assembly process. Appendix B provides appropriate data sheets for material, equipment, and components utilized. Figure 20, Figure 21, Figure 22, and Figure 23 are photographs of the two accelerometers.



Figure 20. Photograph of Dual-Aluminum Disk Accelerometer (NPS3)

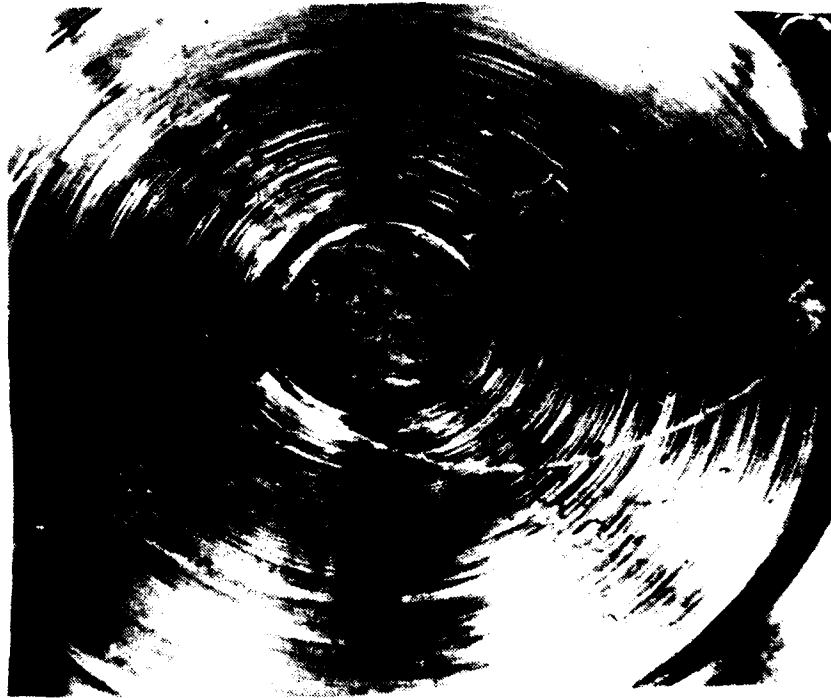


Figure 21. Photograph of Optical Fiber Coil Epoxied to Aluminum Disk (NPS3)

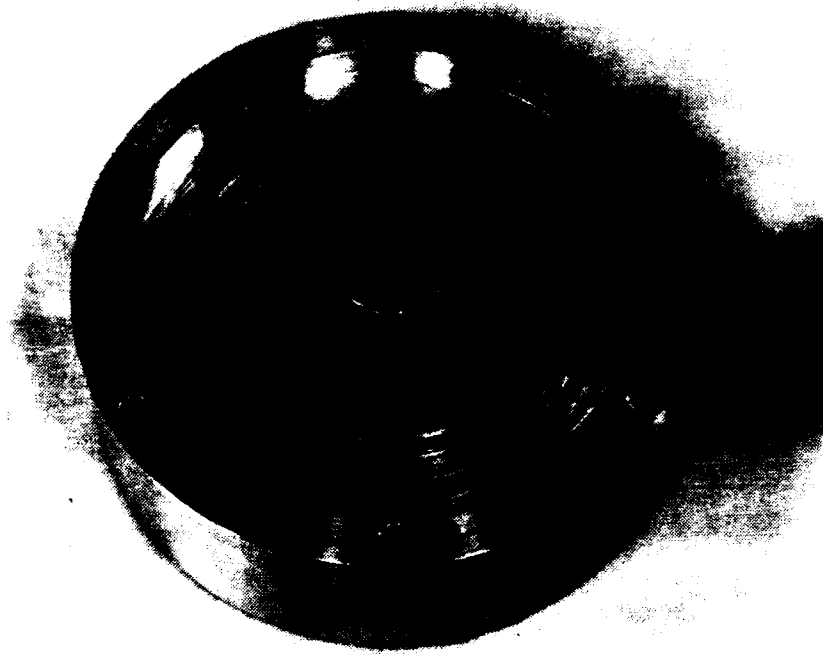


Figure 22. Photograph of Brass Spindel on Bottom Aluminum Disk (NPS3)



Figure 23. Photograph of Polycarbonate Disk Accelerometer (NPS4)

Table 10. OPTICAL FIBER COMPONENTS: All optical fiber had an outer diameter, D , of $250\ \mu\text{m}$; the index of refraction was assumed to be $n = 1.48$.

Optical Components	NPS3 Design	NPS4 Design
Outer coil radii, c	0.028 m	0.029 m
Inner coil radii, b	0.0076 m	0.0075 m
Calculated coil length, L	9.31 m	9.86 m
Measured coil length, L	9.82 m	9.92 m
Optical Fiber	125 μm , 810 nm <i>Coreguide</i> [®]	125 μm , 810 nm <i>Coreguide</i> [®]
2x2 Coupler	Amphenol 945-999-1327, SN 14500	Amphenol 945-999-1377, SN 22381
3x3 Coupler	SIFAM 33582C, SN 01152	SIFAM 33582C, SN 01154
Laser Diode	Hitachi HL8312E	Hitachi HL8312E
Splice Protectors	Sumitomo Electric, 5.9 cm	Sumitomo Electric, 4.0 cm

Table 11. MECHANICAL CHARACTERISTICS: [Refs. 18 , 30].

Property Dimension	NPS3 Design	NPS4 Design
Disk Material	aluminum	polycarbonate
Modulus of Elasticity, Y (GPa)	71.0	2.498
Volume Density, ρ (kg m^3)	2700	1192.9
Poisson's ratio, σ	0.33	0.347
Disk Thickness, t (m)	0.0015	0.001
Disk Radius, a (m)	0.031	0.031

C. PERFORMANCE MEASUREMENT PROCEDURES

1. Resonance Frequency Measurement

The resonance frequency for each design was measured at various stages in the construction process. Measurements were made for each disk while attached to its

housing base with six screws. For the NPS3 design, the resonance frequency was also determined for disk-spindle-disk assembly. After the fiber coils were epoxied to the disk surfaces, the sensor's resonance frequency was measured.

Figure 24 is a block diagram of the apparatus used to measure the resonance frequencies by tapping the disk with the end of a wooden spoon. The impulse free decay response of the sensor or disk was recorded on a Nicolet time-storage oscilloscope [Ref. 10: p. 42]. The number of cycles, N , and the corresponding time length, Δt , were recorded to determine the resonance frequency, $f_0 = \frac{N}{\Delta t}$. The resonance frequency was also determined by measuring the spectrum impulse response with the HP3562A Digital Spectrum Analyzer.

The resonance frequency for the NPS4 design was also determined by placing the sensor on the Bruel & Kjaer shaker table which was driven with random noise. The power spectrum of the photodetector output was exponentially averaged on an HP 3562A Digital Spectrum Analyzer, but really should have been averaged with peak-hold averaging. This method is not truly a linear frequency response of the system; however, it provides information on resonance of the sensor. [Ref. 11: p. 96] (Figure 25)

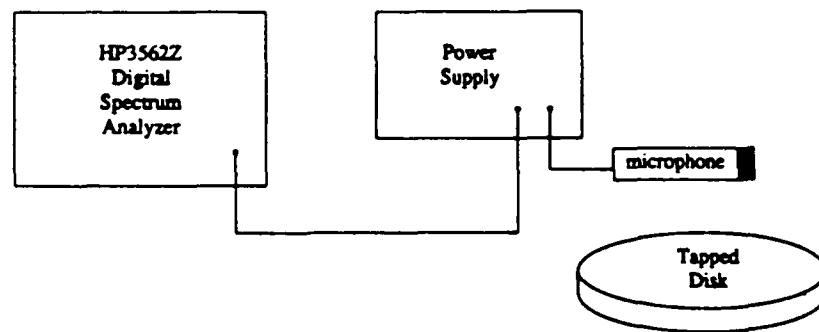


Figure 24. Apparatus to Measure The Resonance Frequency: This apparatus was used to measure the resonance frequency by measuring the spectrum impulse response with the HP3562A. An impulse free decay response method of determining the resonance was also made with this apparatus by incorporating a Nicolet time-storage oscilloscope.

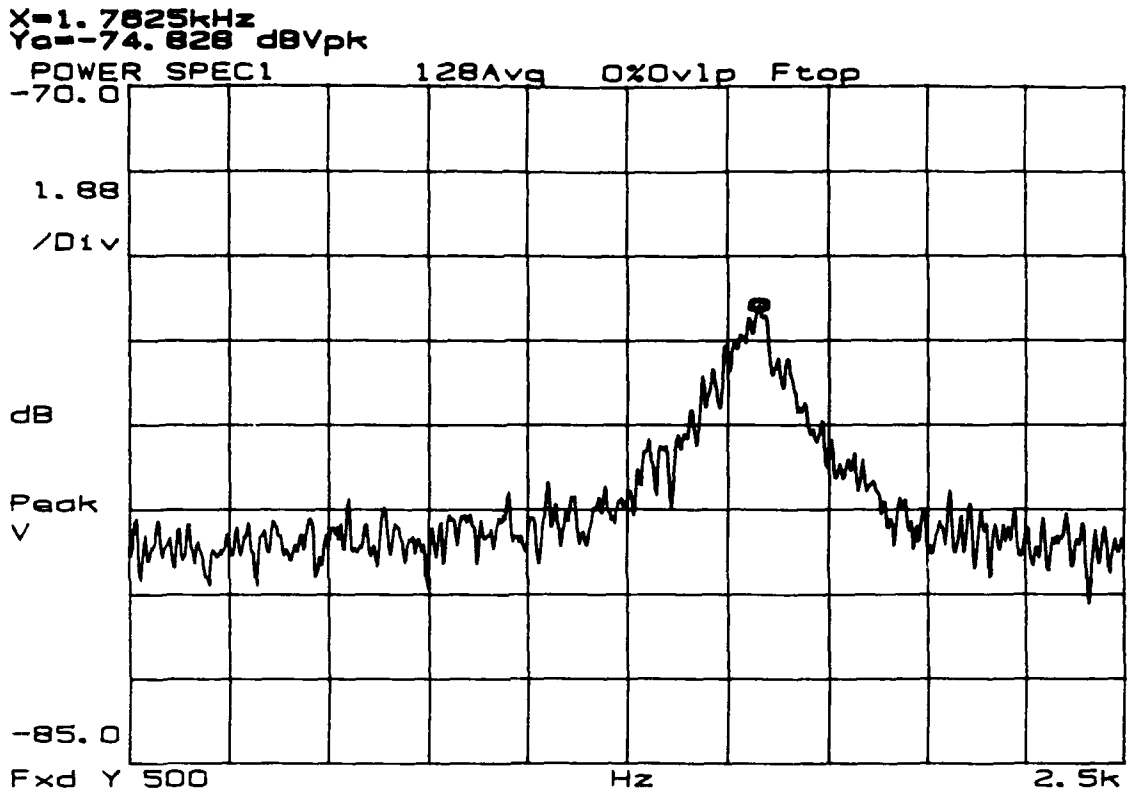


Figure 25. **Photodetector Response Measurement Induced Phase Modulations:** This HP3562A measurement indicates that the resonance frequency is 1.7 kHz and Q is approximately four. The reader is cautioned that exponential averaging was used instead of peak-hold averaging, and thus the signal appears excessively noisy.

2. Acceleration Sensitivity Measurement

An Endevco Model 2215E accelerometer, S/N PN 25, was used as a reference to determine the acceleration sensitivity of both fiber-optic designs. The 2215E calibration sheet indicated the accelerometer has a sensitivity of 187.3 pc/g with a maximum transverse sensitivity of 3.8%, and a bandwidth of 10 kHz. The accelerometer and cable has a total capacitance of 10.8 nf. The voltage sensitivity can be calculated according to,

$$q = CV, \quad (3.1)$$

where q is the charge, C is the capacitance of the accelerometer, and V is the corresponding voltage.

The 2215E acceleration sensitivity was verified by the "chatter" method [Ref. 4: p.18-14]. A steel ball bearing was placed on the Bruel & Kjaer Type 4801 shaker

table as shown in Figure 26. The driving source level was increased until "chattering" of the steel ball against the metal surface of the 4801 vibration table was audible and observed as a distortion of the accelerometer output monitored on an oscilloscope; this corresponded to one "g" of acceleration. The 2215E's observed acceleration sensitivities for 1.0 kHz and below were found to be within 1.5% of the calibrated sensitivity provided in the data sheet; this sensitivity was additionally verified by using the Bruel & Kjaer accelerometer calibrator. With an amplifier gain of 100, an Endevco 2215E acceleration sensitivity of $1.748 V/g$ is used for calculations in the remainder of this thesis.

The Endevco 2215E and the NPS sensor were attached with tackiwax to a Bruel & Kjaer Type 4801 shaker table using a Bruel & Kjaer Type 2712 power amplifier, and was driven by a HP3562A Spectrum Analyzer. The 2215E's peak voltage was measured and the number of visible fringes from the NPS sensor determined; it was convenient to adjust the driving signal's source level such that an integral number of fringes were visible for one half cycle of the 2215E's voltage output (Figure 27 and Figure 28).

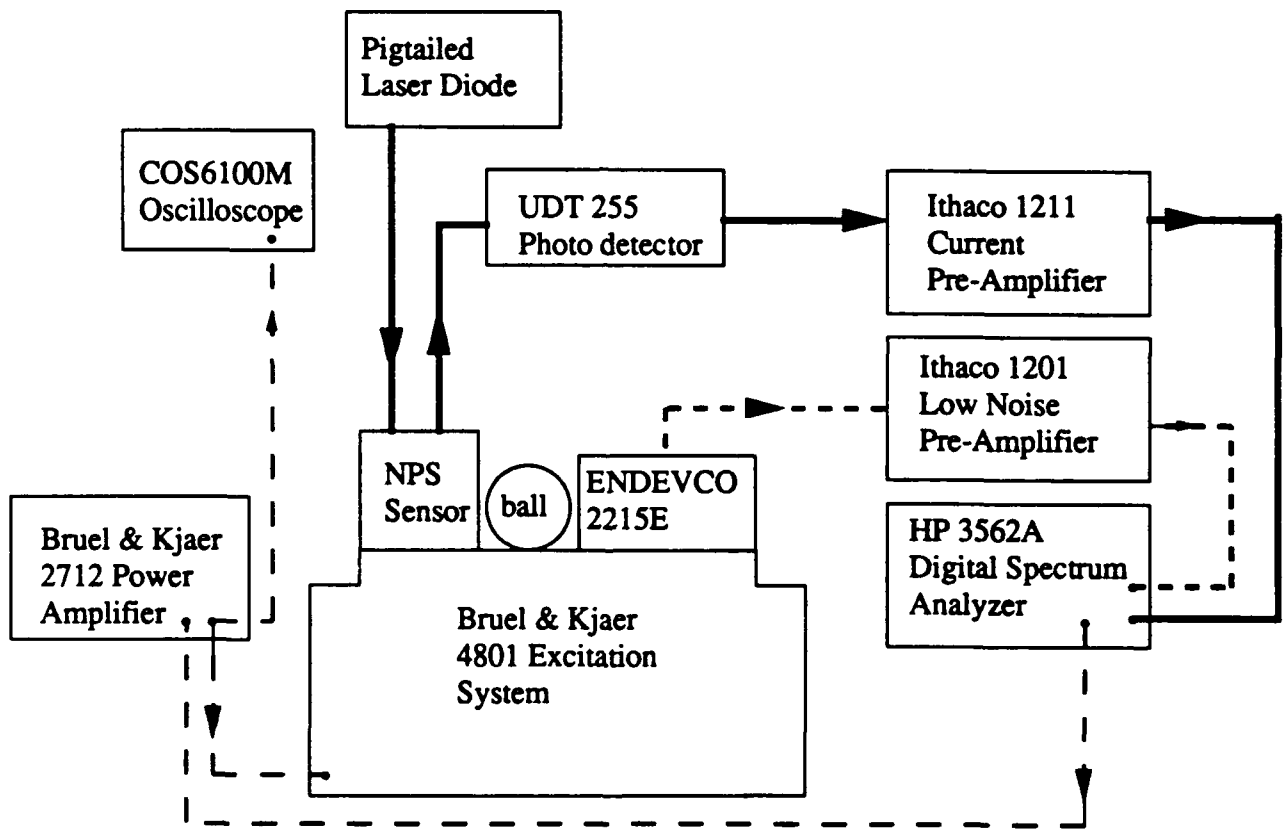


Figure 26. Apparatus Used to Measure the Acceleration Sensitivity

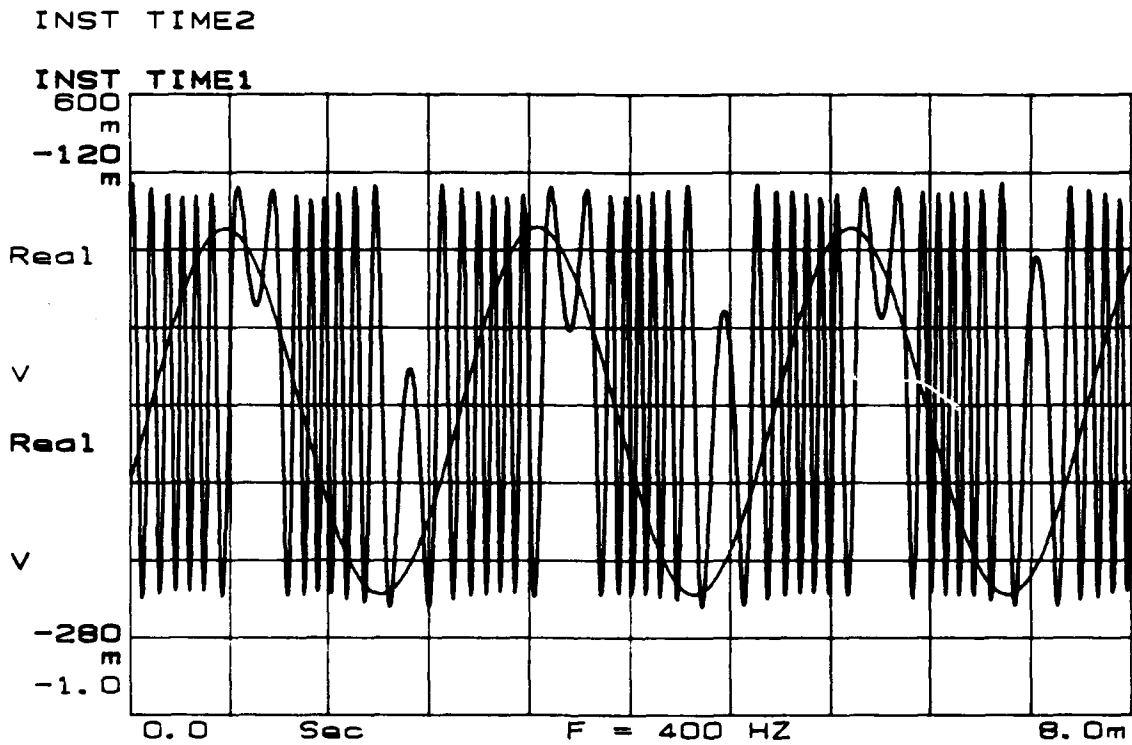


Figure 27. Acceleration Sensitivity Measurement, NPS3: The Endevco 2215E sinusoidal voltage output is superimposed upon the interferometric output from one 3x3 leg of the accelerometer. Seven pk-pk fringes are visible in one-half cycle Endeveco 2215E, yielding an optical acceleration sensitivity of 2.3 rad/g at 400 Hz.

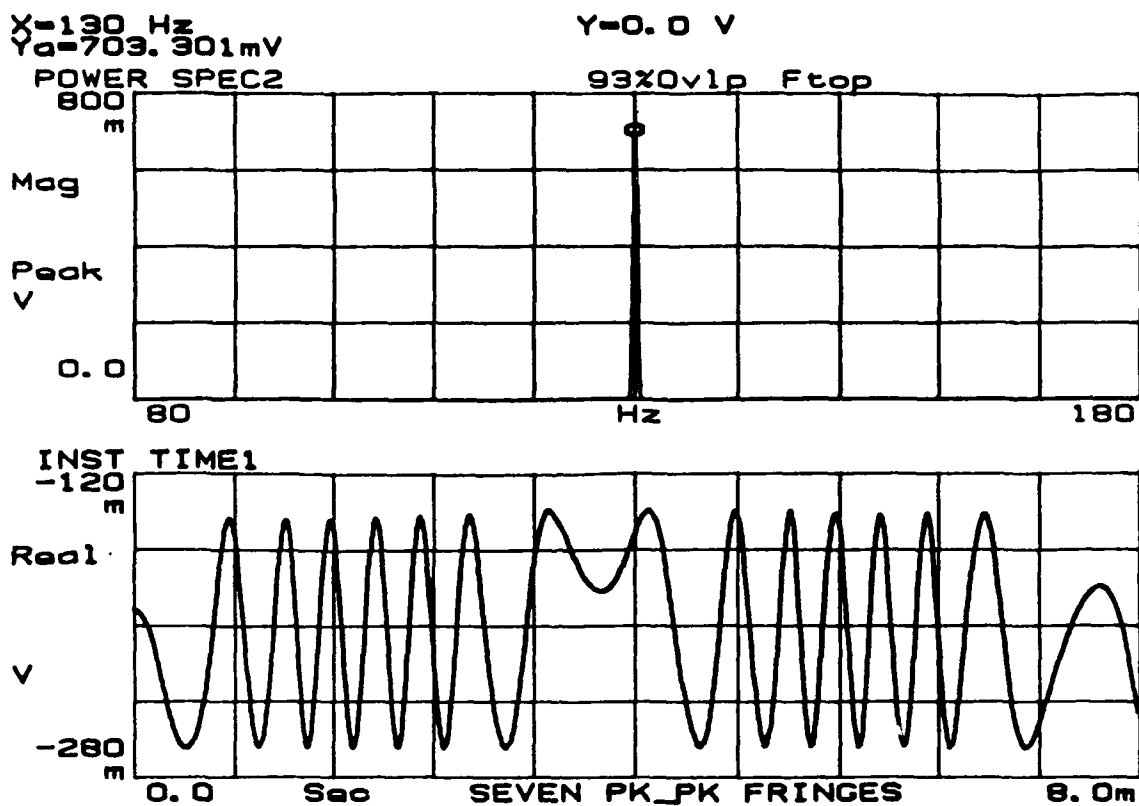


Figure 28. Acceleration Sensitivity Measurement, NPS4: The upper trace is the power spectrum of the Endevco 2215E accelerometer. Seven fringes were visible in one half cycle of the Endevco 2215E signal at 130 Hz. The measured optical acceleration sensitivity was 54.4 rad/g.

D. OBSERVED PERFORMANCE

1. Dual Aluminum Disk (NPS3) Design

The average resonance frequency of the two aluminum disks, both with and without a spindle, was measured to be 2.16 ± 0.07 kHz; these measurements agreed with the theoretically predicted value of >2.07 kHz for the simply supported case. This suggests that the edge conditions are elastically restrained, tending towards a simply supported condition rather than a clamped condition.

The resonance frequency of the completely assembled sensor was expected to be greater than 2.16 kHz since the mass of the epoxied fiber coils added to the disk-spindle assembly formed a mass ratio, $\gamma = 0.7$, which was less than 1.8. The resonance was measured to be 1.22 ± 0.05 kHz and did not agree with theory. The combined effects of the spindle, the four small holes drilled in the bottom disk, and the potential inadvertent placement of epoxy or RTV such that disk displacement was restricted *may* have caused the disparity between the observed and predicted resonance frequency.

Clamped and simply supported boundary conditions predict the acceleration sensitivity to be 0.4 and 2.7 rad g, respectively. Since the resonance frequency of the disk-spindle assembly suggested that the edge conditions tend to the simply supported case, the acceleration sensitivity was expected to have a value closer to 2.7 rad g than to 0.4 rad g. The acceleration sensitivity was measured to be 2.3 ± 0.1 rad g. The sensitivity curve was normalized for illustrative purposes by dividing the sensitivities by 2.3 rad g and is plotted against the frequency ratio (frequency divided by the resonance frequency, 1.22 kHz) shown in Figure 29. Figure 30 shows the normalized sensitivity and a theoretical curve for a Q of 10. The $M_{N,ac}f_0$ figure of merit for the NPS3 accelerometer is 0.03×10^{-9} s/m, or -45 dB re 1 s/m, where s/m is seconds per meter.

A secondary resonance of unknown origin appears at approximately 650 Hz. This secondary resonance was not observed in resonance frequency testing without the bonded fiber optical-fiber coils and reduced the usable bandwidth to less than 450 Hz.

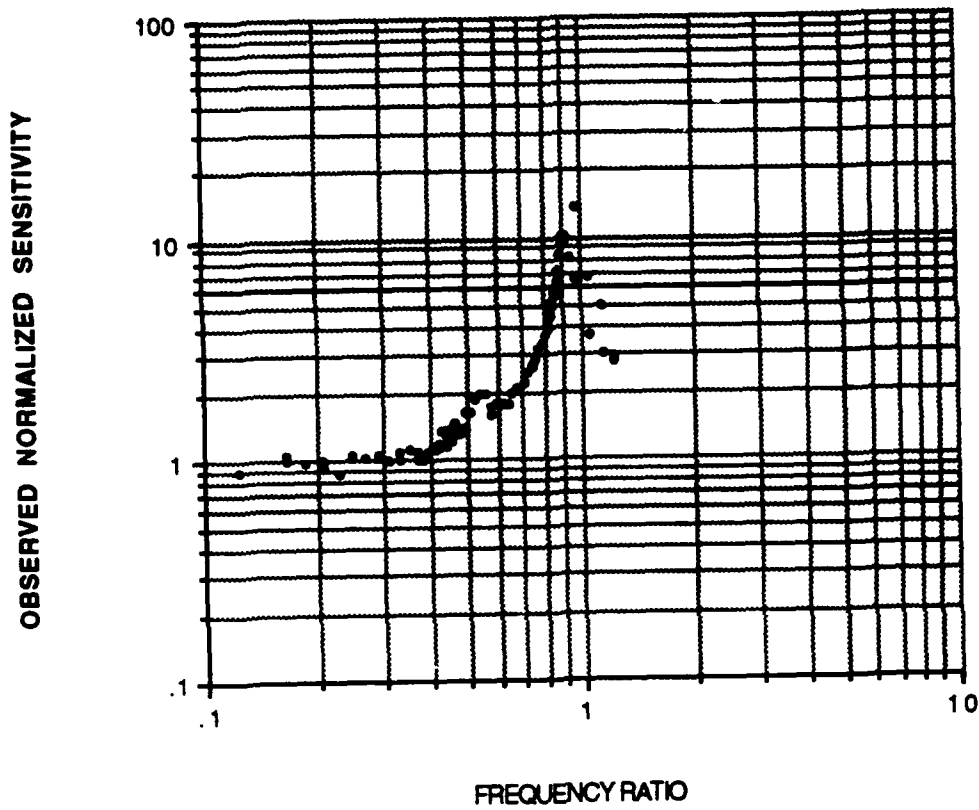


Figure 29. **Normalized Acceleration Sensitivity, NPS3:** The observed normalized sensitivity has no units as it was obtained by dividing all observed sensitivity values by 2.3 rad g. The frequency ratio was obtained by dividing the resonance of 1.22 kHz into frequency.

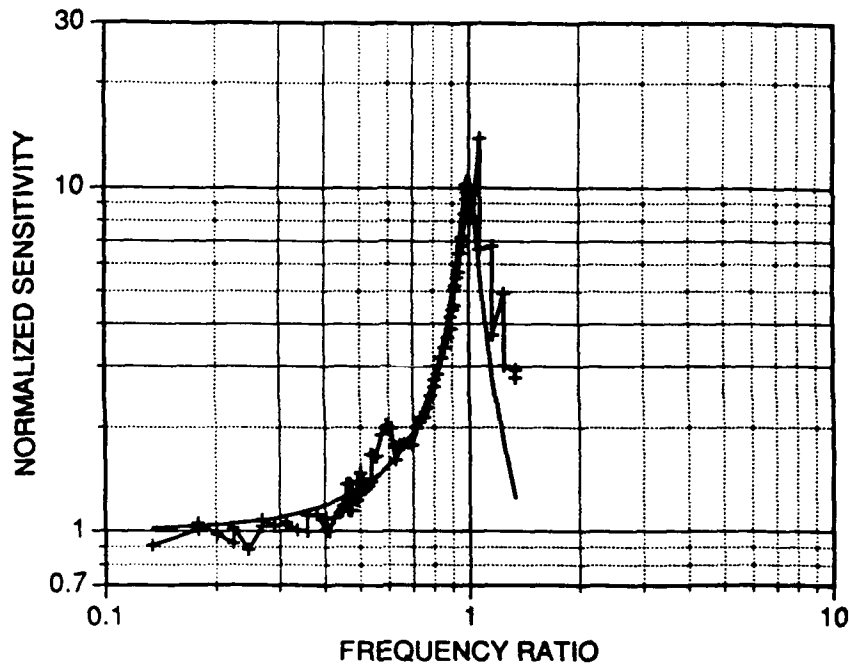


Figure 30. **Normalized Acceleration Sensitivity with Theory, NPS3:** The normalized sensitivity is plotted versus the frequency ratio, as in Figure 29. A theoretical curve corresponding to a Q of 10 is provided.

2. Polycarbonate Disk (NPS4) Design

The lowest observed resonance of the polycarbonate disk was 1029 ± 10 Hz. It is possible that the 1,1 mode, predicted to be 1028 Hz for the simply supported case, was more dominant than the "breathing" (0,1) mode. The lowest expected mode was the 0,1 mode, where a nodal circle exists at the edge boundary, and was predicted to be 366 and 753 Hz for the simply supported and clamped boundary conditions respectively. Figure 31 shows the 0,1 and 1,1 modes. It may be plausible that the two 1.0 mm holes in the polycarbonate disk caused a nodal line to exist, causing the 1,1 mode to dominate.

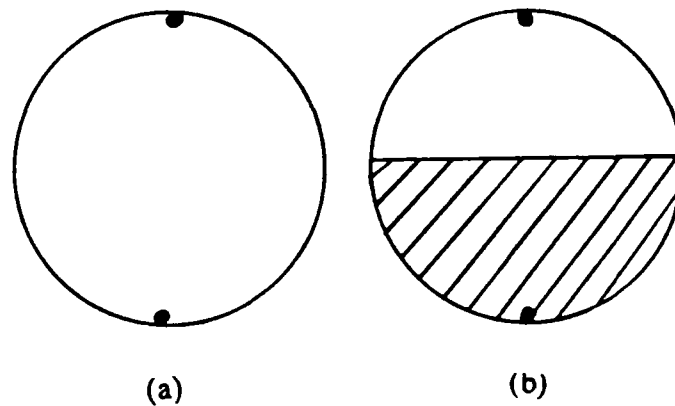


Figure 31. Two Modes of Vibration of a Disk: Two small holes in the disk are depicted by * . (a) The fundamental 0,1 or "breathing" mode is shown in which the displacement of the entire disk is in phase. (b) The 1,1 mode is illustrated. The nodal line across the disk diameter causes the displacement of each disk half to 180 ° out of phase. [Ref. 18]

The completely assembled NPS4 accelerometer had a resonance frequency of 1.7 ± 0.5 kHz and a Q of approximately 4. Since the disk's mass ratio, $\gamma = 0.7$, is less than 1.8, the observed resonance was expected to be greater than 367 Hz for the simply supported 0,1 mode, greater than 1028 Hz for the simply supported 1,1 mode, and greater than 753 Hz for the clamped 0,1 mode. The observed resonance suggests that the disk edge condition realized was more simply supported than clamped and that the 1,1 mode was more easily observed than the 0,1 mode.

The observed sensitivity was 56.9 ± 4.0 rad g over the bandwidth of 30-950 Hz. The sensitivity curve was normalized for illustrative purposes by dividing the sensitivities by 56.9 rad g and is plotted against the frequency ratio (frequency divided by the resonance frequency 1.7 kHz) shown in Figure 32. Figure 33 shows the normalized sensitivity and a theoretical curve for a Q of 4. The $M_{N,ac} f_0$ figure of merit for the NPS4 accelerometer is 0.9×10^{-3} s, m, or -30 dB re 1 s'm.

If the 1,1 mode was truly the dominant mode of the disk, then the acceleration sensitivity would be expected to be small. The surface strains on each half of the disk surfaces, induced by acceleration, would be 180 ° out of phase and would effectively cancel. The cause of this inconsistency is as yet unexplained.

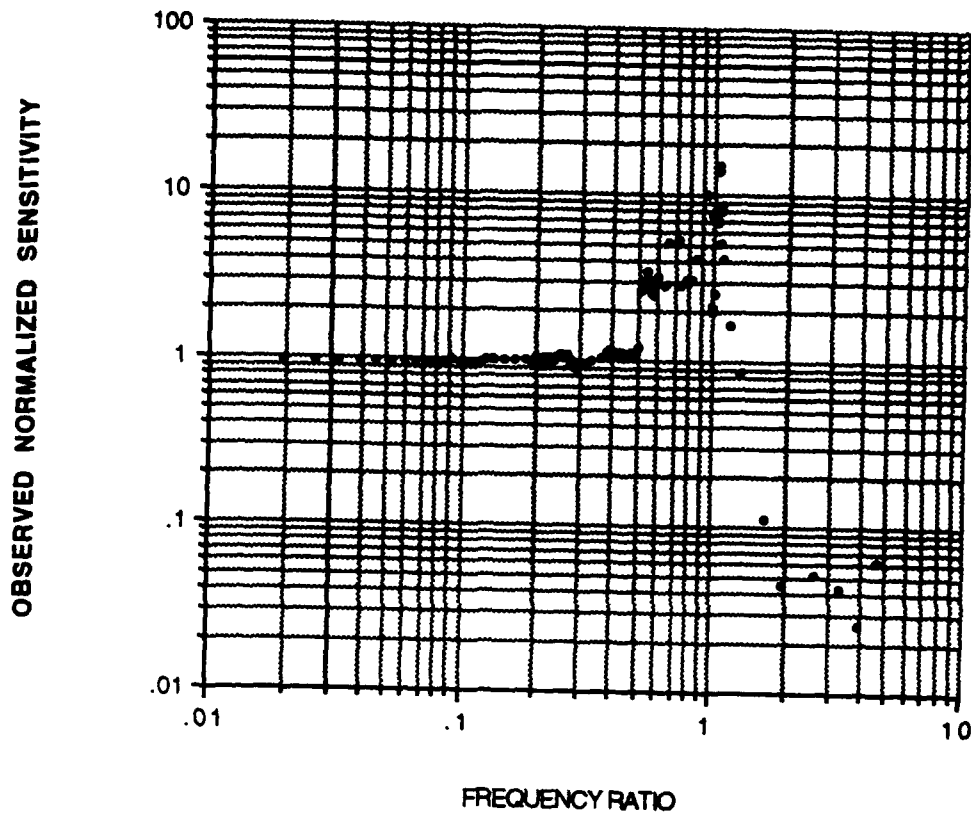


Figure 32. Normalized Acceleration Sensitivity, NPS4: The observed normalized sensitivity has no units as it was obtained by dividing all observed sensitivity values by 56.9 rad g. The frequency ratio was obtained by dividing the resonance of 1.7 kHz into frequency.

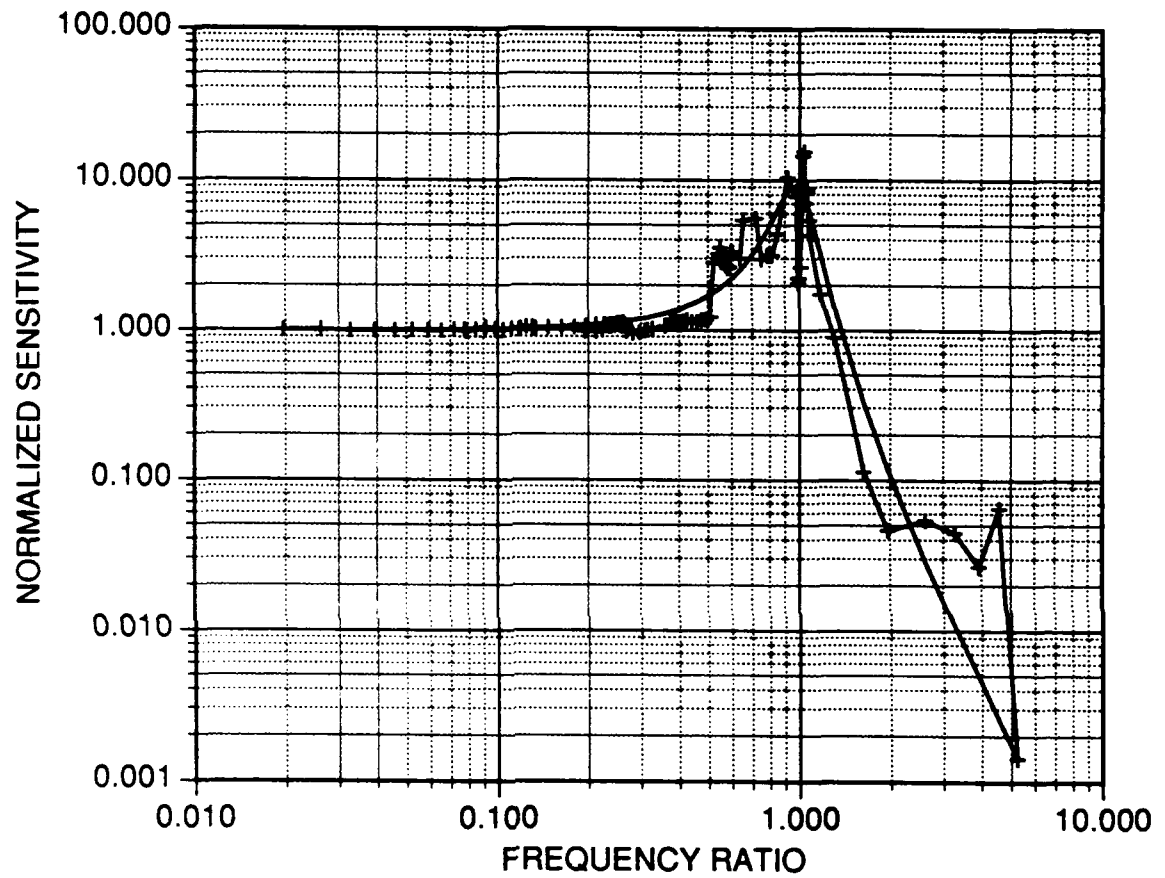


Figure 33. **Normalized Acceleration Sensitivity with Theory, NPS4:** The normalized sensitivity is plotted versus the frequency ratio, as in Figure 32. A theoretical curve corresponding to a Q of 4 is provided.

IV. CONCLUSIONS AND RECOMMENDATIONS

A. CONCLUSIONS

1. Performance

The figure of merit, $M_N f_0$, provides the best direct comparison of fiber-optic accelerometer performance; this figure of merit is dimension-independent, depending only on the physical properties of the transducing material. The NPS3 and NPS4 accelerometers had $M_N f_0$ figures of merit of -45 and -30 dB re 1 s/m, respectively. Table 12 provides comparison of the two accelerometer designs of this thesis with the two designs previously built at the Naval Postgraduate School. The rubber mandrel NPS1 design had the best $M_N f_0$ figure of merit at -15 dB re 1 s/m and the NPS2 flexural disk design had the largest usable bandwidth.

The first design of this thesis, the NPS3 design, had an acceleration sensitivity of 2.3 ± 0.1 rad/g over a bandwidth of 475 Hz, and a resonance frequency of 1.22 ± 0.05 kHz. The NPS1 and NPS2 designs had $M_N f_0$ products which were respectively, 30 and 18 dB better than the NPS3 design. Although the NPS3 had an operational bandwidth almost twice that of the NPS1 design, the NPS1 sensor had a sensitivity which was 5,000 times greater.

The second sensor of this thesis, the NPS4 design, improved the $M_N f_0$ product by a factor of thirty over the NPS3 design. This design had a resonance frequency of 1.7 ± 0.5 kHz and an acceleration sensitivity of 56.9 ± 4.0 rad/g over a bandwidth of 950 Hz. The usable bandwidth of 950 Hz is the largest of the four fiber optic accelerometers built at NPS. The NPS4 sensor had a $M_N f_0$ product of 0.9 s/m, which is 15 and 3 dB less than the NPS1 and NPS2 designs, respectively.

2. Design Concerns

The dual aluminum disk (NPS3) design had several features which prevented confident and thorough predictions of performance. Foremost among these is that the disks were of non-uniform thickness. The boundary conditions appeared to be more simply supported than clamped. The observed sensitivity of 2.3 rad/g was 15% less than sensitivity predicted for the simply supported condition and was 155% greater than the sensitivity predicted for the clamped condition. Similarly, the resonance frequency of 1.22 kHz was more indicative of the simply supported case. A conclusive reason to ex-

Table 12. COMPARISON OF ACCELEROMETER PERFORMANCES: [Refs. 2, 7, 14]

Parameter	Units	NPS1	NPS2	NPS3	NPS4
Design Type		Michelson	Michelson	Mach-Zender	Mach-Zender
M_{cc}	dB re 1 rad g	90	17	3	17
M_{cc}	rad g	10,000	49	2	56
$M_{N,ac}$	1 g 10 ⁶	120	0.9	0.02	0.5
f_0	Hz	240	2450	1220	1700
L	m	7.4	5	9.3	9.9
ϕ	rad 10°	83	56	107	113
BW	Hz	240	800	450	950
$M_{N,ac}f_0$	s m 10 ³	29	2	0.03	0.9
$M_{N,ac}f_0$	dB re 1 s m	-15	-27	-45	-30

plain why the sensor's resonance frequency was 1.22 kHz instead of being greater than 2.07 kHz was not obtained.

The second design of this thesis was much simpler and provided clearer predictions of performance. The boundary condition appeared to be more simply supported than clamped. The observed sensitivity of 56.9 rad/g was 5% greater than the sensitivity predicted for the simply supported condition and was 87% greater than the sensitivity predicted for the clamped condition. The 1,1 mode appeared more dominant than the

fundamental 0,1 mode during resonance frequency testing; the 0,1 mode was never observed. It is perplexing that the acceleration sensitivity was relatively high when the 1,1 mode appeared to describe the disk's flexural motion. One would expect the sensitivity to be small if the 1,1 mode were dominant.

It is important in the research and design process to keep the design plans simple and understandable, and to progressively approach greater complexity in design. Additionally, the fiber optic design must weigh several limiting factors such as the minimum optical-fiber bend radius, the dimensions of available couplers and splice protectors, and the advantages of completely housing all optical components.

B. RECOMMENDATIONS

For future flexural disk accelerometer designs, it is recommended that materials such as polycarbonate or *Stycast*[®]1266, which have lower sound speeds than aluminum, be used. The figure of merit $M_{N,ac}f_0$ is inversely proportional to the material's speed of sound. The lower the sound speed, the higher the acceleration sensitivity will be.

To maximize the transduction of induced strain to the coiled optical fiber, an improved design might have multiple layered coils of optical fiber epoxied in two disks. The epoxied coils would serve as the "flexural disks." A modification of this design might include the two or more separate coils of multiple layers being interwound and epoxied in on simple disk. [Ref. 33]

An optimum shape should be determined. Flexural disks are easily made and are convenient to incorporate into designs. However, alternative shapes having maximum strain distributions where the maximum amount of optical fiber is present may be more advantageous. Flexural disks have a maximum strain distribution at the center; however, the critical bend radius of optical fiber precludes the winding of coils to exploit the maximum strain at the disk center. [Ref. 11]

APPENDIX A. SENSOR ASSEMBLY AND PACKAGING

A. INTERFEROMETER ASSEMBLY

Sensor assembly begins with the fabrication of a Mach-Zender interferometer. In each step summarized below, careful attention is necessary when measuring fiber lengths and light intensities, and when preparing fiber ends for splicing.

1. The fiber coils were prepared for assembly .
 - a. NPS3: Both fiber ends of each coil were fed through the four holes in the lower disk and through heat shrink splice protectors.
 - b. NPS4: Both fiber ends of one coil were fed through two holes in the polycarbonate disk. Individual splice protectors were used at each splice in the interferometer.
2. An operating laser was spliced to one 2x2 input fiber; the remaining input fiber is not utilized.
3. Spliced one 2x2 output fiber to the outer fiber end of coil 1.
4. Spliced the remaining 2x2 output fiber to the outer fiber end of coil 2.
5. Spliced the inner fiber end of coil 2 to a 3x3 input fiber.
6. Spliced the inner fiber end of coil 1 to a second 3x3 input fiber; the third input fiber was trimmed to a convenient length and was not utilized.
7. NPS3: The pre-positioned heat shrink splice protectors were heated.

B. SENSOR PACKAGING

The assembly process continues with the packaging of the interferometer.

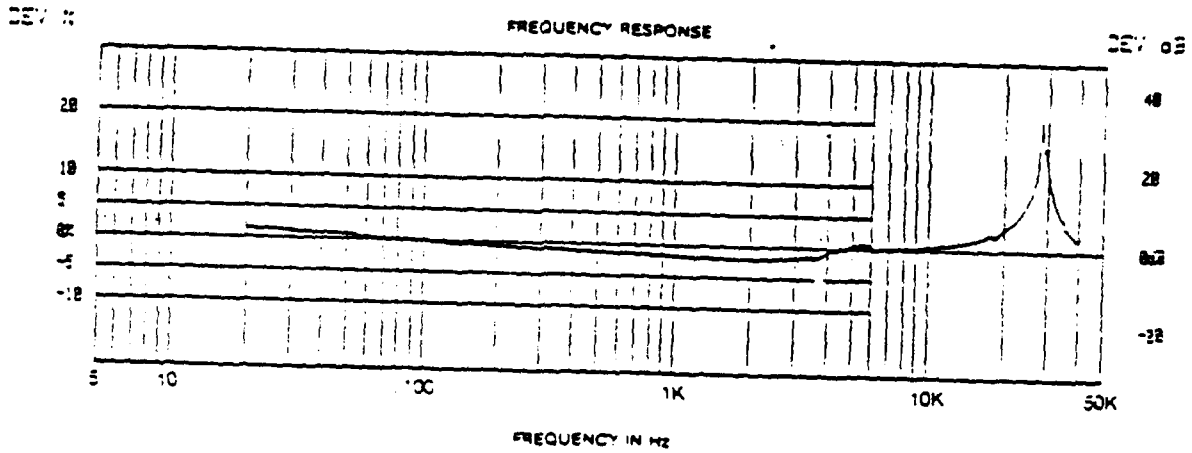
1. The disk surfaces to which the coils are applied were gently rubbed with fine grit paper to improve epoxy adhesion, and were thoroughly cleaned with alcohol.
2. Excess rubber cement was carefully removed from each coil with alcohol and tweezers.
3. *Stycast*[®] 1266 epoxy was mixed and degassed in a vacuum chamber.
4. The two couplers, splice protectors, and excess fiber were placed in the base. In the NPS4 design, the couplers partially extended through the base side port.
5. The disk surfaces were lightly "wetted" with epoxy.
 - a. NPS3: Both coils were placed on their respective disk surfaces, flattened, and covered with a small quantity of epoxy.

- b. NPS4: One coil was placed on the bottom disk surface, was flattened, and covered with a small quantity of epoxy.
6. In approximately 20 minutes the epoxied coils were tacky.
- a. NPS3: RTV was generously placed in the base to prevent the couplers, splice protectors, and fiber from moving. The spindle ends were lightly covered with tackiwax, and the sensor was assembled with the tightening of the six sockethead screws.
 - b. NPS4: A second batch of *Stycast*[®] 1266 epoxy was prepared. The second coil was epoxied to the disk's top surface in a manner similar to the first coil. *Ecosil*[®] 4592, a silicon epoxy, was mixed, degassed, and generously placed in the base; the sensor was assembled with the attachment of the protective cap with six sockethead screws.
7. The epoxies were permitted to cure overnight before sensor testing commenced.

APPENDIX B. DATA SHEETS

Calibration Data

ACCELEROMETER MODEL 2215E SERIAL NO 2425
 Sensitivity 187.3 gC/g @ 100 Hz 18.95 gK
 MAXIMUM TRANSVERSE SENSITIVITY: 3.8 g
 CAPACITANCE @ 100 1000 pF



Date JUN 24 1988
 By [Signature] ENDEVCO 
 ALL CALIBRATIONS ARE PERFORMED UNDER NATIONAL BUREAU OF STANDARDS AND IN ACCORDANCE WITH MIL-STD-883C. THE
 CENTER HAS THE ACCREDITED STATUS OF THE PERFORMANCE ORGANIZATION AND PROVIDES CALIBRATED INSTRUMENTS
 THROUGHOUT THE WORLD.



Canton, Mass. 02021 (617) 628-3300 (710) 346-1324
 Gardena, Calif. 90248 (213) 321-6650 (910) 346-6736
 Northbrook, Ill. 60062 (312) 272-6700 (810) 686-0006

Emerson & Cuming, Inc.

DIELECTRIC MATERIALS DIVISION
 CANTON, MASSACHUSETTS

TECHNICAL BULLETIN 7-2-26C

STYCAST® 1266

Transparent High Impact Room Temp. Cure Epoxy Casting Resin

STYCAST 1266 is a clear, low viscosity casting resin which when fully cured has outstanding toughness and impact strength. STYCAST 1266 can be cured at room temperature.

STYCAST 1266 has been used for display embedments. It has been used to bond lenses and sheets of glass for good visibility. STYCAST 1266 has good moisture resistance, electrical properties and adhesion to metal, glass and plastics. After catalyst addition, viscosity at room temperature is extremely low, making it easy to pour. Vacuum processing is not always needed. It will readily impregnate windings.

Long exposure of the cured resin to temperatures above 250°F (121°C) will cause some discoloration. Physical and electrical properties are not appreciably affected.

Typical Properties:

Mixed Viscosity at 77°F (25°C), cps	650
Specific Gravity	1.18
Hardness, Shore D	75
1/2 in. Impact, ft. lbs. / in. (kg. cm. / cm.) of notch	2 (11)
Compressive Strength, psi (kg/cm ²)	10,000 (700)
Tensile Strength, psi (kg/cm ²)	6,000 (422)
Volume Resistivity, ohm-cm	6 x 10 ¹⁴
Dielectric Strength, volts/mil (kv/mm)	400 (15.8)
Dielectric Constant, at 10 ⁷ Hz	3
Dissipation Factor, at 10 ⁶ Hz	0.02
Flexural Strength, psi (kg/cm ²)	20,000 (1,406)
Index of Refraction	1.56

4650 cat price

Instructions for Use:

1. Prepare materials and mold for use.
2. Add 28 parts of Part B to 100 parts by weight of Part A. Mix thoroughly. Pot life will be about 1/2 hour. Use small batches. Use multiple pouring for castings over 100 grams.
3. Pour. Use vacuum evacuation if necessary.
4. Allow to stand at room temperature for 8 hours. The casting can be removed from mold when hard. A post cure at 200°F (93°C) for 2 hours will increase the hardness of the cured resin and its dielectric strength.
5. Curing at temperatures of 125°F to 150°F (51°C to 66°C) to speed production is possible, and depends both on resin mass, and the geometry of the unit to be potted. To determine optimum conditions, user should run a few experiments on the particular unit.

The handling of this product should present no problems if ordinary care is exercised to avoid breathing vapors, if the skin is protected against contamination, if swallowing is avoided, and if the eyes are protected. We recommend observing the precautions in Public Health Service Publication No. 1040, May 1967, which is available from the Superintendent of Documents, U. S. Government Printing Office, Washington D. C. 20402.

The shelf life of this product is 6 months when stored in sealed, unopened containers at temperatures no higher than

This information, while believed to be completely reliable, is not to be taken as warranty for which we assume legal responsibility nor as permission or recommendation to practice any patented invention without license. It is offered for consideration, investigation, and verification.

ECCOSIL 5877

HIGH-STRENGTH SILICONE FOR MOLD MAKING, PROTOTYPE TOOLING

Eccosil 5877 is an easily pourable, addition curing silicone used to make prototype tooling, flexible molds, rollers and mandrels for electroforming and embossing. It can be used with most thermosets—epoxies, polyesters, urethanes, low melting metals, plasters and waxes. Eccosil 5877's low viscosity allows it to form thin, intricate molds with excellent reproduction of detail. Its flexibility and high tear strength permit multiple uses.

Eccosil 5877 has a convenient 10:1 by weight mix ratio for ease in weighing and mixing, and can be cured rapidly at elevated temperatures for fast turnaround time in manufacturing. It should be noted that this material can be cured over a wide range of temperatures without adversely affecting the material's properties.

Eccosil Primer S-11 is recommended for use with Eccosil 5877 to improve adhesion to nonsilicone materials and to minimize the probability of cure inhibition from surface contaminants on nonsilicone substrates.

KEY FEATURES

- Excellent Reproduction of Detail
- High Tear Strength
- Fast Cure at Elevated Temperatures
- Reversion Resistance
- Noncorrosive
- 10:1 Mix Ratio

TYPICAL PROPERTIES

HANDLING PROPERTIES:

Color	Red
Mix Ratio by Weight, A/B	10/1
Viscosity Part A, at 25°C, cps	30,000
Part B, at 25°C, cps	350
Mixed, at 25°C, cps	15,000
Cured Specific Gravity, g/cc	1.40
Pot Life, Min. at 25°C	30
Gel Time, Min. at 25°C	120
Initial Cure, Hrs. at 100°C	1
Post Cure, Hrs. at 175°C	2
Shelf Life, Months	6

PHYSICAL PROPERTIES:

Hardness, Shore A	.65
Tensile Strength, psi	800
Tensile Elongation, %	100
Tear Strength, pli	.40
Cure Shrinkage, cm/cm	<.002

THERMAL PROPERTIES:

Coefficient of Thermal Expansion, per °C	3×10^{-4}
Thermal Conductivity, Cal/cm ² /°C/sec/cm	7×10^{-4}
Glass Transition Temp., °C	-120
Service Temp., Upper Limit, °C	250
Lower Limit, °C	-60

ELECTRICAL PROPERTIES:

Dielectric Strength, volts/mil	450
Volume Resistivity, at 25°C, ohm-cm	1×10^{14}
Dielectric Constant, 1MHz	3.5
Dissipation Factor, 1MHz	0.01

TECHNICAL BULLETIN

**EMERSON
& CUMING**
A GRACE COMPANY

INSTRUCTIONS FOR USE:

1. Mix the contents of both Part A and Part B in their original shipping containers. Weigh out the desired amount of Eccosil 5877 in a mixing vessel. For each 100 parts of Eccosil 5877, Part A, add 10 parts of Eccosil 5877, Part B.
2. Mix thoroughly. Power mixing is preferred to make sure that both parts have been thoroughly blended.
3. Evacuate the resin mixture to remove entrapped air.
4. Pour catalyzed material into the mold.
5. The Eccosil 5877 may be cured over a broad range of temperatures. After 24 hours at room temperature, it will be hard enough to handle. Optimum properties will be achieved after 7 days. The Eccosil 5877 can be cured rapidly at elevated temperatures, even in thick sections. A typical elevated cure is 1 hour at 100°C, followed by a post cure at 175°C for 2 hours to ensure full properties.

NOTE: Cure may be inhibited through contact with certain contaminants. Common materials which should be avoided are sulfur or sulfur containing materials, nitrogen containing materials, RTV silicone catalysts, and heavy metal salts. Molds, mixing equipment, ovens and other apparatus that will be used in the preparation and curing of Eccosil 5877 should be free of inhibiting contaminants.

HYGIENE:

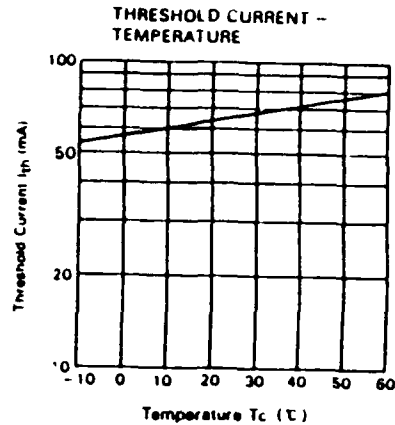
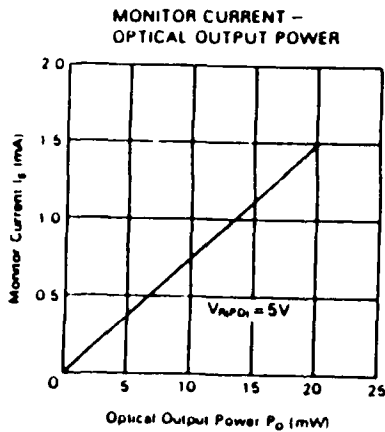
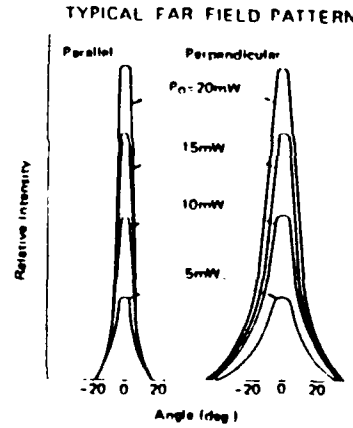
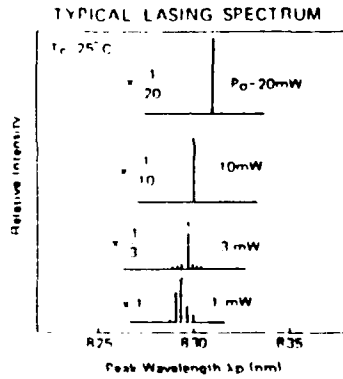
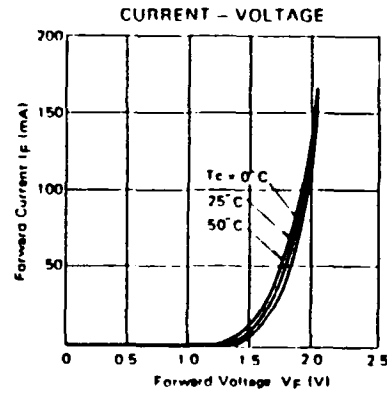
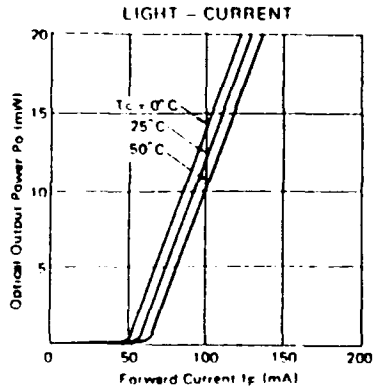
The handling of this material should present no problems if ordinary care is exercised to prevent breathing of vapors, if the skin is protected against contamination, if swallowing is avoided and if the eyes are protected.

WARRANTY: This information is, to the best of W.R. Grace & Co.'s ("Grace") knowledge, accurate as of the date indicated. This information relates only to the specific material designated herein and is not intended for the application or use of the material with any other material or in any process. The information is intended as a general guide only and does not constitute a warranty or representation whatsoever and GRACE HEREBY DISCLAIMS ALL EXPRESS AND IMPLIED WARRANTIES ARISING FROM THE USER'S RELIANCE ON OR USE OF THIS INFORMATION.

**EMERSON
& CUMING**
Where there's a way.

• OPTICAL AND ELECTRICAL CHARACTERISTICS (Tc=25°C)

Item	Symbol	Test Condition	HLB312E			Unit
			min	typ	max	
Threshold Current	I_{th}		-	60	90	mA
Optical Output Power	P_O	Kink free	20	-	-	mW
Slope Efficiency	η		0.16	0.28	-	mW/mA
Peak Wavelength	λ_p		810	830	850	nm
Beam Divergence Parallel to the Junction	$\theta_{//}$	$P_O = 10\text{mW}$	-	10	-	deg
Beam Divergence Perpendicular to the Junction	θ_{\perp}		-	27	-	
Monitor Current	I_s	$V_{APD} = 5\text{V}, P_O = 10\text{mW}$	0.2	-	-	mA
Rise and Fall Time	t_r, t_f		-	-	0.5	ns



HL8312E

GaAlAs LD

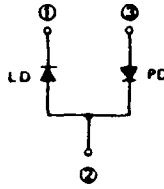
APPLICATIONS

- Optical memory disc.
- Laser beam printer.
- Light source for any other optical equipment.

FEATURES

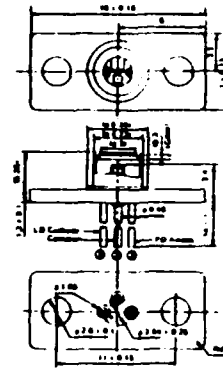
- Wavelength between 810 and 850nm.
- Photodetector built in for monitoring.
- Continuous and pulsed wave operation up to 20mW at room temperature.
- Stable fundamental transverse mode.
- Single longitudinal mode.
- Fast pulse response. t_r and t_f are less than 0.5 ns.
- High reliability.

PACKAGE



The photodetector built in for power monitoring simplifies and automatic power control circuit

PACKAGE DIMENSIONAL OUTLINE (Dimensions in mm)

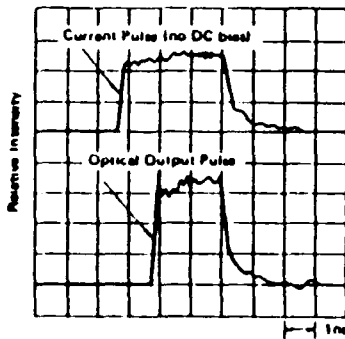


ABSOLUTE MAXIMUM RATINGS (Tc=25°C)

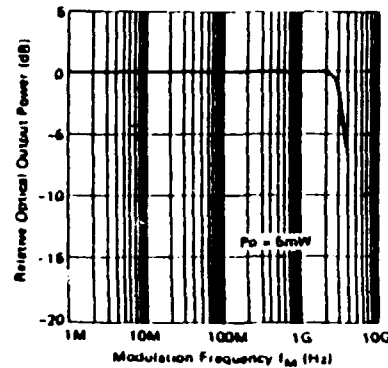
Item	Symbol	HL8312E	Unit
Optical Output Power	P_o	20	mW
Laser Diode Reverse Voltage	$V_{R(LD)}$	2	V
Photo Diode Reverse Voltage	$V_{R(PD)}$	30	V
Operating Temperature	T_{opr}	-10 ~ +50	°C
Storage Temperature	T_{stg}	-40 ~ +80	°C

HL8312E

PULSE RESPONSE



FREQUENCY RESPONSE



LIST OF REFERENCES

1. Cameron, C. B., Keolian, R. M., and Garrett, S. L., "A Symmetric Analogue Demodulator for Optical Fiber Interferometric Sensors," *34th Midwest Symposium on Circuit and Systems (IEEE)*, Monterey, California, May 14-17, 1991.
2. Brown, D. A., and Garrett, S. L., "An Interferometric Fiber Optic Accelerometer", *Fiber Optic and Laser Sensors VIII*, Proc. Soc. Photo-Optical Inst. Engr. (SPIE), 1367, 283-288, 1990.
3. Magrab, E. B. and Shinaishin, O. Q., *Vibration Testing-Instrumentation and Data Analysis*. The American Society of Mechanical Engineers, New York, 1975.
4. Harris, C. M. and Crede, C. E., *Shock and Vibration Handbook*, Second Edition, McGraw-Hill Book Company, New York, 1976.
5. Wilson, O. B., *Introduction to Theory and Design of Sonar Transducers*. Peninsula Publishing, Los Altos, California, 1988.
6. Thomson, W. T., *Theory of Vibration With Applications*, Third Edition, Prentice Hall, Englewood Cliffs, New Jersey, 1988.
7. Gardner, D. L., *A Fiber-Optic Interferometric Seismic Sensor With Hydrophone Applications*, Doctoral Thesis in Engineering Acoustics, SN ADB112487, Naval Postgraduate School, Monterey, California, 1987.
8. Powers, J.P., *An Introduction to Fiber Optic Systems*, pending publication, Monterey, California 1992.
9. Davis, C. M., "Fiber Optic Sensors: An Overview," *Optical Engineering*, **24**, 347-351, Mar-Apr, 1985.

10. Brown, D. A., *A Fiber-Optic Flexural Disk Hydrophone*, Master's Thesis in Engineering Acoustics, SN ADB132243, Naval Postgraduate School, Monterey, California, 1989.
11. Brown, D. A., *Optical Fiber Interferometric Acoustic Sensors Using Ellipsoidal Shell Transducers*, Doctoral Thesis in Engineering Acoustics, SN B158605, Naval Postgraduate School, Monterey, California, 1991.
12. Tventen, A. B., Dandridge, A., Davis, C. M., and Giallorenzi, T. G., "Fiber Optic Accelerometer," *Electronic Letters*, 16,854-856, 1980.
13. Davis, C. M., Eustace, J. G., Zarobila, C. J., and Rogers, P. W., "Fiber Optic Seismometer", *Fiber Sensors II*, Proc. Soc. Photo-Optical Inst. Engr. (SPIE), September 1986.
14. Olcott, J. E., *Fiber-Optic Flexural Disk Accelerometer*, Master's Thesis in Engineering Acoustics, SN A246203, Naval Postgraduate School, Monterey, California, 1991.
15. Adler, U., *Automotive Handbook*, Eighteenth Edition, Robert Bosch Company, Germany, 1976.
16. Timoshenko, S., Woinowsky-Kreiger, S., *Theory of Plates and Shells*, Second Edition, McGraw-Hill Book Company, New York, 1959.
17. Young, W. C., *Roark's Formulas for Stress and Strain*, Sixth Edition, McGraw-Hill Book Company, New York, 1989.
18. Kinsler, L. E., Frey, A. P., Coppens, A. B., and Sanders, J. V., *Fundamentals of Acoustics*, Third Edition, Wiley, New York, 1982.
19. Leissa, A. W., *Vibration of Plates*, NASA Tech Doc: SP-160-N70-18461, Washington, DC, 1969.

20. Handelman, G. and Cohen, H., *On the Effects of the Addition of Mass to Vibrating Systems*, U.S. Air Force Tech Doc: AFOSP TN - 56 - 387, Rensselaer Polytechnic Institute, Troy, New York, 1956.
21. Huang, C. L. D. and Huang, S. T., "Finite Element Analysis of Non-Linear Vibration of a Circular Plate with a Concentric Rigid Mass," *Journal of Sound and Vibration*, **131**(2), 215-227, 1989.
22. Gutierrez, R. H., Laura, P. A. A., and Grossi, R. O., "Transverse Vibrations of Plates with Stepped Thickness Over a Concentric Circular Region," *Journal of Sound and Vibration*, **69**(2), 285-295, 1980.
23. Laura, P. A. A., Luisoni, L. E., and Arias, A., "Antisymmetric Modes of Vibration of a Circular Plate Elastically Restrained Against Rotation and Subjected to a Hydrostatic State of In-Plane Stress," *Journal of Sound and Vibration*, **47**(3), 433-437, 1976.
24. Juarez, J. A. G., "Axisymmetric Vibrations of Circular Plates With Stepped Thickness," *Journal of Sound and Vibration*, **26**(3), 411-416, 1973.
25. Avalos, D., Laura, P. A. A., and Bianchi, A. M., "Analytical and experimental investigation on vibrating circular plate with stepped thickness over a concentric circular region," *J. Acoust. Soc. Am.*, **82**(1), 13-16, 1987.
26. Avalos, D., Laura, P. A. A., and Larrondo, H. A., "Vibrating circular plate with stepped thickness over a concentric circular region A general, approximate solution," *J. Acoust. Soc. Am.*, **84**(4), 1181-1185, 1988.
27. Laura, P. A. A., and Gutierrez, R. H., "Transverse Vibration of Annular Plates of Variable Thickness With Rigid Mass on Inside," *Journal of Sound and Vibration*, **79**(2), 311-315, 1981.
28. Gelos, R., Ficcadenti, G. M., Grossi, R. O., and Laura, P. A. A., "Vibrations of circular plates with variable profile," *J. Acoust. Soc. Am.*, **65**(5), 1326-1329, 1981.

29. Wetterskog, K., Beaton, B. L., and Serocki, J., *A Fiber-Optic Acceleration Canceling Hydrophone Made of a Castable Epoxy*, Master's Thesis in Engineering Acoustics, SN ADB46067 Naval Postgraduate School, Monterey, California, 1989.
30. Bartlett, D. L., *Determination of the Complex Elastic Moduli of Materials Using a "Free-Free" Bar Technique*, Master's Thesis in Engineering Acoustics, Naval Postgraduate School, Monterey, California, 1992.
31. Brown, D. A., Cameron, C. B., Keolian, R. M., Gardner, D. L., and Garrett, S. L., "A Symmetric 3x3 Coupler Based Demodulator for Fiber Optic Interferometric Sensors," *Fiber Optic and Laser Sensor IX*, (SPIE) Paper 1584-41, Naval Postgraduate School, Monterey, California, 1991.
32. Cameron, C. B., *Recovering Signals from Optical Fiber Interferometric Sensors*, Doctoral Thesis in Electrical Engineering, SN EC-91-005, Naval Postgraduate School, Monterey, California, 1991.
33. Brown, D. A., Personal Conversation, Naval Postgraduate School, Monterey, California, December 1991.

INITIAL DISTRIBUTION LIST

	No. Copies
1. Defense Technical Information Center Cameron Station Alexandria, VA 22304-6145	2
2. Library, Code 52 Naval Postgraduate School Monterey, CA 93943-5002	2
3. CDR, Dr. D. L. Gardner, NOAA Dept. of Physics (Code PH) Naval Postgraduate School Monterey, CA 93943	3
4. Dr. D. A. Brown Dept. of Physics (Code PH) Naval Postgraduate School Monterey, CA 93943	3
5. Prof. S. L. Garrett Dept. of Physics (Code PH) Naval Postgraduate School Monterey, CA 93943	3
6. Prof. A. A. Atchley Dept. of Physics (Code PH) Naval Postgraduate School Monterey, CA 93943	1
7. LT M. B. A. Chipkevich, USN Department of the Navy Space and Naval Warfare Systems Command ATTN: LT M. B. A. Chipkevich, USN (PMW 183) Washington, DC 20363-5100	1